Towards designing elastic and magnetic properties of Co-based thin film metallic glasses

Von der Fakultät für Georessourcen und Materialtechnik der

Rheinisch-Westfälischen Technischen Hochschule Aachen

zur Erlangung des akademischen Grades einer

Doktorin der Ingenieurwissenschaften

genehmigte Dissertation

vorgelegt von **M.Sc.**

Carolin Hildegard Hostert

aus Aachen

Berichter: Univ.-Prof. Jochen M. Schneider, Ph.D.

Professor Dr.-Ing. Dierk Raabe

Tag der mündlichen Prüfung: 06. Juli 2012

Materials Chemistry Dissertation

No.: 17 (2012)

Carolin Hostert

Towards designing elastic and magnetic properties of Co-based thin film metallic glasses

ABSTRACT

The fact that metallic glasses combine both metallic properties and characteristics of amorphous materials lead to intensive research worldwide, exploring this interesting class of materials. Co-based metallic glasses, and $Co_{43}Fe_{20}Ta_{5.5}B_{31.5}$ in particular, offer the attractive combination of both high fracture strength and excellent soft magnetic properties. Within the framework of this thesis, the generation, validation and implementation of a first principles model for $Co_{43}Fe_{20}Ta_{5.5}X_{31.5}$ (X=B,Si,P,S) metallic glasses are described. This model allows for the identification of valence-electron-concentration and size-induced changes in structure, elastic and magnetic properties and hence contributes towards a knowledge based design of metallic glasses in the future.

Within the generated *ab-initio* model stoichiometric body centered cubic supercells are assumed as initial configurations. After annealing at 4000 K, all cells were quenched down to 0 K at different cooling rates and subsequently relaxed in terms of atomic positions and volumes. To validate this first principles model, density and elastic modulus as well as the pair distribution function and volume magnetization of sputtered Co-Fe-Ta-(B/Si) thin film metallic glasses were measured. The computationally obtained density and stiffness values as well as the theoretical pair distribution function of Co-Fe-Ta-B and the volume magnetization of the Si-containing alloy are consistent with experimental data obtained for thin films and with literature data. The infinite cooling rate to quench the molten alloy was determined to be sufficient.

The implementation of the for Co-Fe-Ta-(B/Si) successfully validated first principles model was realized by analyzing short range order, charge transfer and the bonding nature by means of density of states, Bader decomposition and pair distribution function analysis. For $Co_{43}Fe_{20}Ta_{5.5}X_{31.5}$ (X=B,Si,P,S) a clear trend of a decrease in density and bulk modulus as well as a weaker cohesion was observed as the valence electron concentration for the X element is increased by replacing B with Si and further with P and S. This observed trend upon X variation may be understood based on increased interatomic distances, variations in coordination numbers and the electronic structure changes: As the valence electron concentration of X is increased, the X bonding becomes more ionic. This factor disrupts the overall metallic interactions and leads to weaker cohesion and stiffness. Density of states as well as pair distribution functions are used to identify (Co,Fe)-X atomic pairs as the shortest and strongest constituents. These strong bonds may give rise to a comparatively large stiffness. The highest magnetic moments – and the largest population of unpaired transition metal

Abstract

d-states – are identified for X=S, despite the fact that the presence of X generally reduces the magnetic moment of Co. The interplay between transition metal d-band filling and s-d hybridization was hence identified to be a key materials design criterion. Furthermore, an extended diagonal relationship between the B- and P-containing amorphous alloys (in coherence to the known relationship between elements of the second and third period) was revealed.

This thesis indicates that systematic quantum mechanics simulations enable the identification of composition-induced changes in short range order, charge transfer and bonding nature of metallic glasses. These characteristics are correlated with density, elasticity and magnetism. The here identified property-electronic structure correlations may thus provide the basis for future knowledge based design of glassy materials.

ZUSAMMENFASSUNG

Die Tatsache, dass metallische Gläser sowohl Eigenschaften klassischer Metalle als auch die Charakteristika amorpher Werkstoffe in sich vereinen, führte zu einer intensiven Erforschung dieser interessanten Materialien weltweit. Co-basierte Gläser im Allgemeinen und die Legierung $Co_{43}Fe_{20}Ta_{5.5}B_{31.5}$ im Speziellen zeichnen sich dabei durch eine attraktive Kombination von hoher Bruchfestigkeit bei gleichzeitig exzellenten weichmagnetischen Eigenschaften aus. Im Rahmen dieser Doktorarbeit wird die Generierung, Validierung und Implementierung eines *ab-initio* Modells für metallische Gläser der Art Co-Fe-Ta-X (X=B,Si,P,S) beschrieben. Mit Hilfe dieses Modells konnten erfolgreich Einflüsse der Valenzelektronenkonzentration sowie der Größe des X-Elements auf Struktur, elastische und magnetische Eigenschaften identifiziert werden. Der hier vorgestellte Ansatz kann so zu einem zukünftigen, wissensbasierten Design von metallischen Gläsern beitragen.

Das generierte *ab-initio* Modell beruht auf der Annahme, dass stöchiometrische, kubisch-raumzentrierte Superzellen die Anfangskonfiguration wiedergeben. Einer Glühung bei 4000 K folgt die Abschreckung auf 0 K (mit verschiedenen Abkühlraten), gefolgt von einer Relaxation hinsichtlich Atompositionen und Volumina. Experimentell bestimmte Werte der abgeschiedenen Co-Fe-Ta-(B/Si) Dünnschichtgläser sowie Literaturdaten dienen der Validierung des hier vorgestellten *ab-initio* Modells. Die Dichten und Steifigkeiten, sowie die Paarverteilungsfunktion (Co-Fe-Ta-B) und Volumenmagnetisierung des Si-haltigen Glases stimmen sowohl mit den experimentell ermittelten Daten als auch mit Literaturangaben überein. Dabei stellte sich die unendlich schnelle Abschreckung der schmelzflüssigen Legierung als hinreichend heraus.

Die anschließende Implementierung des für das System Co-Fe-Ta-(B/Si) erfolgreich validierten Modells wird für das System $Co_{43}Fe_{20}Ta_{5.5}X_{31.5}$ (X=B,Si,P,S) durch eine Nahordnungs-, Ladungstransfer- und Bindungszustandsanalyse mittels Zustandsdichten und Paarverteilungsfunktionen sowie einer Bader-Zerlegung realisiert. Steigt die Valenzelektronenkonzentration des X-Elements (dies tritt ein, wenn B nach und nach jeweils vollständig durch Si, P und S ersetzt wird), ist ein klarer Trend hin zu einer verminderten Dichte, eines verminderten Kompressionsmoduls und zu schwächerer Kohäsion beobachtbar. Dieser Trend könnte auf vergrößerten Atomabständen, Veränderungen in der Koordinationszahl und der elektronischen Struktur basieren: Mit zunehmender Valenzelektronenkonzentration für X wird der Bindungscharakter von Bindungen, an denen X beteiligt ist, ionischer. Dieser Umstand wiederum

Zusammenfassung

unterbricht die sonst vorherrschende metallische Interaktion der Atome untereinander und führt zu einer niedrigeren Kohäsion und Steifigkeit. Sowohl die Zustandsdichten als auch die Paarverteilungsfunktionen deuten darauf hin, dass (Co,Fe)-X Paare die Bestandteile des Glases sind, die die kürzesten und stärksten Bindungen aufweisen und so die recht hohen Steifigkeiten erklären könnten. Die größten magnetischen Momente – und die meisten ungepaarten d-Zustände innerhalb der Übergangsmetalle – wurden für X=S gefunden. Nichtsdestotrotz kann die Aussage getroffen werden, dass das Vorhandensein eines X-Elements das magnetische Moment für Co generell reduziert. Das Zusammenspiel von Übergangsmetall d-Schalenbesetzung und s-d Hybridisierung scheint daher einer der Schlüsselfaktoren für ein erfolgreiches Materialdesign auf dem Gebiet der metallischen Gläser zu sein. In der hier vorgestellten *ab-initio* Studie wurden darüber hinaus Ähnlichkeiten zwischen den Gläsern mit X=B und P gefunden, was mit einer erweiterten diagonalen Schrägbeziehung zwischen B und P (analog zu der bekannten Schrägbeziehung zwischen Elementen der zweiten und dritten Periode) zusammenhängen könnte.

Diese Doktorarbeit zeigt, dass zusammensetzungsinduzierte Veränderungen in der Nahordnung, des Ladungstransfers und des Bindungszustands mit Hilfe von systematischen, auf quantenmechanischen Simulationen basierenden Untersuchungen identifiziert werden können. Da dieser Ansatz die Korrelation mit materialspezifischen Eigenschaften wie Dichte, Elastizität und Magnetismus beschreibt, stellt er die Grundlage für ein zukünftiges, wissensbasiertes Design von glasartigen Materialien dar.

PREFACE

This thesis contains work done by the author at Materials Chemistry, RWTH Aachen University, Germany from April 2007 to December 2011. This includes planning and realization of thin film depositions and analysis, generation and implementation of the computational model by *ab-initio* simulations and calculations as well as writing three articles.

SQUID and XRR measurements were conducted by the Materials Physics Group, Uppsala University, Sweden. X-ray diffraction experiments using high-energy photons were conducted at Deutsches Elektronen Synchrotron DESY by J. Bednarcik. The compositional analysis of the thin films were carried out by CAMECA and Imago. These collaborations are gratefully acknowledged.

The thesis is based on the following articles:

1. Hostert C., Music D., Bednarcik J., Keckes J., Kapaklis V., Hjörvarsson B. and Schneider JM. Ab-initio molecular dynamics model for density, elastic properties and short range order of Co-Fe-Ta-B metallic glass thin films. Journal of Physics: Condensed Matter 2011;23:475401

2. Hostert C., Music D., Kapaklis V., Hjörvarsson B. and Schneider JM. Density, elastic and magnetic properties of Co-Fe-Ta-Si metallic glasses by theory and experiment. Sripta Materialia 2012;66:765-768

3. Hostert C., Music D., Bednarcik J., Keckes J. and Schneider JM. Quantum mechanically guided design of $Co_{43}Fe_{20}Ta_{5.5}X_{31.5}$ (X=B,Si,P,S) metallic glasses. Journal of Physics: Condensed Matter 2012;24:175402

Acknowledgements

TABLE OF CONTENT

LIST OF ABBREVIATIONS AND SYMBOLS

ATP	atom probe tomography
BMG	bulk metallic glass
CPU	central processing unit
DC	direct current
DFT	density functional theory
DOS	density of states
DSC	differential scanning calorimetry
GFA	glass-forming ability
GGA	general gradient approximation
LDA	local density approximation
MEMS	micro electro mechanical systems
NI	nanoindentation
OpenMX	Open source package for Materials Explorer
PDF	pair distribution function
PVD	physical vapor deposition
RF	radio frequency
SRO	short range order
SQUID	superconducting quantum interference device
UHV	ultra high vacuum
UV	ultra violett
VASP	Vienna Ab-Initio Simulation Package
XRD	X-ray diffraction
XRR	X-ray reflectivity

$A_p(h_c)$	projected indentation area
$\langle b \rangle$	average scattering power of the sample
b_i	scattering power of atom i
B	bulk modulus
c_i	atomic concentration
d	lattice plane spacing
d_{ij}, r_{ij}	mean nearest neighbor distance

List of Abbreviations and Symbols

E	Young's modulus
E_r	reduced Young's modulus
ϵ	energy eigenvalue
$f_i(q)$	scattering factors of the atomic species
$g(r)$	pair distribution function
$G(r)$	reduced pair distribution function
h_c	contact depth
H	Hamiltonian operator
$-\dfrac{\hbar^2}{2m}\nabla^2$	kinetic energy operator
$I_e(q)$	normalized elastically scattered intensity
m	electron mass
n	integer
N_{ij}/N_{ji}	coordination number
r	radial distance
r_{ion}	ionic radius
$R(Q)$	reflectivity
R_{ij}	Goldschmidt's radius
S	stiffness
$S(q)$	total structural factor
$U(\mathbf{r}_i, \mathbf{r}_j)$	electron-electron interaction energy
U_{tot}	total energy of probed configuration
$V(\mathbf{r})$	potential energy
$V_H(\mathbf{r})$	Hartree potential
$V_{XC}(\mathbf{r})$	exchange-correlation potential
w_{ij}	X-ray weighting factor calculated at $q=0$ Å^{-1}
Z	effective charge of the ion
β	geometrical constant
θ	diffraction/reflection angle
λ	X-ray wavelength
ν	Poisson's ratio
ρ	density

$\rho(r)$	local atomic number density
ρ_0	average atomic number density
$\rho_e(z)$	average density profile
ρ_∞	bulk density
σ	standard deviation
σ_y	elastic limit
Φ	ionic potential
ψ	wavefunction
$\psi_i(\mathbf{r})$	single-electron wave function

1 INTRODUCTION

Since metallic glasses combine both metallic properties and characteristics of amorphous materials, much effort has been spent to explore this class of materials. The innate structure of metallic glasses exhibits short range order but is lacking long range order, which is leading to outstanding materials properties.

1.1 DEFINITION OF METALLIC GLASSES

Until the end of the last century metals and metallic alloys were applied in our everyday life and technology mainly in its crystalline form. The fact that metals/alloys were known primarily as crystalline materials can be attributed to characteristics such as easy and fast diffusion processes, leading to immediate nucleation and growth of the crystalline phase as the melt is cooled down. From the Greek wording "*a*" without and "*morphé*" shape/form a definition for another solid modification can be derived: "amorphous": An amorphous material is a material that lacks long range order, as known for crystals, revealing a disordered atomic/molecular structure. For amorphous solids, which are the topic of this thesis, the often used term "glass(y)" originates from the materials history and is defined as a path-dependent quantity: The material has been created via rapid solidification of a melt with suppressed crystallization. Since both terms "amorphous" and "glass(y)" are often used equivalently, another aspect than the materials history is prevalently taken into account to distinguish an "amorphous" solid from a "glass": Materials exhibiting a glass transition should be referred to as "glasses" (see Figure 1-1 for a schematic DSC thermogram and a schematic graph plotting specific volume against temperature of a glassy material).

Introduction
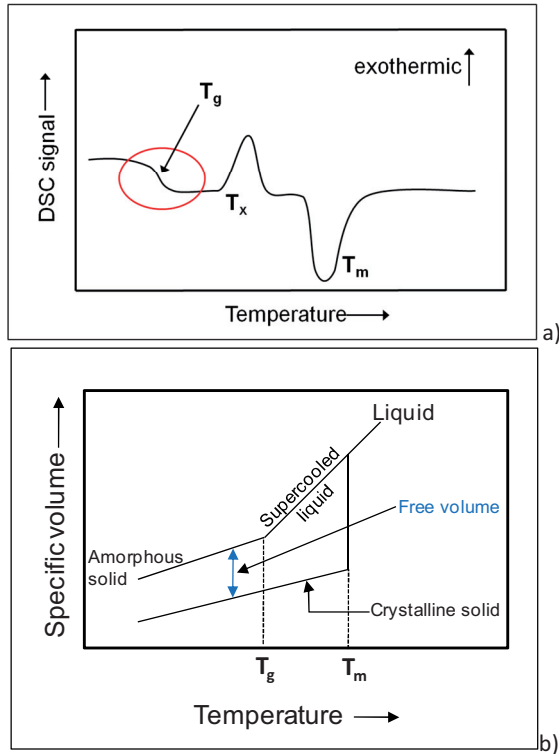
Figure 1-1: *Schematic graphs of a typical DSC thermogram for a glassy material (a) showing thermodynamic events (glass transition temperature T_g, crystallization temperature T_x and melting temperature T_m, respectively) and a plot of specific volume against temperature for an amorphous material (b) showing T_g and T_m, respectively.*

This means that there is a pathway to transform the material into its (supercooled) liquid phase by changing one of the state variables such as temperature or pressure. As a conclusion, one may state that a glass is always amorphous but something amorphous does not necessarily have to be a glass. Since this distinction is not always made in literature, both terms will be used within this thesis to paraphrase the systems under study.

1.2 RESEARCH TRENDS

The exploration of metallic glasses started with investigations on characteristics such as sample size and glass-forming ability: The fact that metals can be quenched to a non-crystalline state was discovered by Duwez et al. in 1960 for a

binary alloy consisting of Au and Si, employing the rapid quenching technique with cooling rates of 10^5-10^6 K/s [1]. The resulting flake had a thickness of ~10 μm. Until that date the amorphous material portfolio mainly consisted of silicates and chalcogenites. For Duwez's system as well as for Turnbull and Chen's splat quenched Pd-Si and Pd-Cu-Si alloys, the presence of a glass transition was proven [2, 3]. Chen and co-workers coined the term "bulk metallic glass" within the aforementioned Pd-Cu-Si alloy and an achieved thickness larger than 1 mm [4]. By constitutional modification of existing alloys and further screening for suitable metallic glass compositions, the reachable diameter where still fully amorphous samples were obtained could be increased to the centimeter scale for $Pd_{40}Ni_{40}P_{20}$ [5] in 1984. The critical size of metallic glass ingots was increased further to above 50 mm for $Pd_{40}Cu_{30}Ni_{10}P_{20}$ [6], even reaching 72 mm [7] in 1997. Hence this important attribute could be improved by more than three orders of magnitude within the last decades. Consequently, the composition dependent improvement of glass-forming ability, exemplified by an increased critical casting thickness, is still in focus of metallic glass design. Nevertheless this is not the only field where improvements were achieved: Inoue et al. identified a high glass forming ability with a supercooled region as high as 70 K within rare-earth containing compounds such as $Al_{20}La_{55}Cu_{25}$ [8], which could be even improved to 135 K in the Zr–Ti–Cu–Ni–Be alloy system by Hays and Johnson [9, 10].

Due to the inherent structure of metallic glasses, which is lacking long range order, grain boundaries and dislocation, specific forming and processing techniques such as blow molding or thermoplastic forming are utilized enabling the identification of new potential fields of application. For example, the supercooled liquid region can be used to employ new processing routes like near-net-shape processing [11] and blow molding [12] to obtain extremely smooth surfaces without the need of post-treatment [13]. Thermoplastic forming without shrinkage upon solidification is reported for the alloy system $Zr_{44}Ti_{11}Cu_{10}Ni_{10}Be_{25}$ [12]. This enables the production of small precision parts or components where reduced wear/energy loss by friction (due to atomistically smooth surfaces) is needed. The fact that grain boundaries are absent acts beneficial on the corrosion resistance and may lead to applications as diaphragms in diaphragm-type MEMS vacuum sensors [14] or to applications which are so far limited by grain size, like the field of re-writable data storage media [15]. The potential to store energy and the high resilience of bulk metallic glasses has already led to applications in e.g. sporting goods [16] (www.liquidmetal.com). Metallic glasses in form of thin films and composites are also of importance: Thin films, mainly deposited by magnetron (co-)sputtering, are either used for a highly efficient property

Introduction

screening [17-24] or are directly aiming for a later application as composite material [25, 26], e.g. as a bilayered structure in the fabrication of high density bit-patterned magnetic recording media [25]. Other forms of composites than i.e. thin film multilayers, are in-situ particle/phase-reinforced BMGs [27, 28] foreign-particle-reinforced BMGs [29-31], or fiber-reinforced BMGs [32, 33], mainly aiming at improving the mechanical properties of monolithic metallic glasses. Magnetic properties such as high saturation magnetization, low coercivity and high effective permeability are of interest for several potential fields of application such as magnetic head cores, thin film inductors, transformer cores as well as quick-response magnetic sensors [18, 34, 35]. A high saturation magnetization is reported for transformer cores where crystalline Fe-Si was replaced by Fe-Si-B metallic glass [34]. The combination with excellent high frequency magnetic properties like those reported for the Fe-Ga-Al-P-C metallic glass [36], may lead to applications as magnetic-shielding sheets for laptop PCs.

1.3 STRUCTURE AND SHORT RANGE ORDER OF METALLIC GLASSES

The fact, that the innate structure of metallic glasses reveals short range order but is lacking long range order is leading to outstanding materials properties [12, 14, 15, 32, 37-41] has already been mentioned before. This short range order depends strongly on composition [42, 43], topology [44, 45] and electronic structure [46], while in turn, SRO impacts on several materials properties such as density [44] (a metallic glass tends to maximize the local density, rather than targeting for a high overall density like it is realized in a closely packed crystal), glass formation [42] and stability [46] (by either supporting the precipitation of the corresponding crystalline phase or suppressing it). For metallic glasses the generic term of "short range order" can be rendered more precisely into two terms denoted as "chemical short range order" and "geometric short range order" [47, 48]. The latter one describes the spatial arrangement and degree of randomness within the system and is furthermore called "topological short range order" [47, 49], while chemical short range order defines nearest neighbor arrays originating from chemical affinity between the components.

Computational methods and the first principles approach in particular offer various and unique opportunities to model and describe SRO, correlate it to the materials properties and to understand the immanent physical mechanisms thereof [50]. Existing computational approaches are the reverse Monte Carlo method [51], (*ab-initio*) molecular dynamics simulations [52-54] or classical molecular dynamics [50]. While reverse Monte Carlo modeling is irretrievably reliant on experimental input such as diffraction data [47], a*b-initio* molecular

dynamics methods are able to draw conclusions *a priori*. Disadvantages of this approach include very short simulation time scales, very high cooling rates, poor statistics and periodic boundary conditions applied to a relatively small unit cell as well as a high demand on computational resources. Since the computational part of this dissertation is based on a*b-initio* molecular dynamics, more information on this method can be found in section 2.

For metallic glasses, as for other materials, these computational approaches offer opportunities for investigating and understanding the immanent physical mechanisms [50] leading to an enhanced glass forming ability [55-59] and underlying, the often discussed structure-property-correlations [60-63], as well as (chemical) short range order [47, 63-68] and dynamic properties [69]. Furthermore, these approaches enable the validation of various phenomenological models existing, describing and attempting to explain the inherent structure of metallic glass alloys [50]: The first established model, employing hard spheres as element representatives, is the "Bernal's Dense Randomly Packed Hard Sphere Model" communicated in 1960 [70]. Due to the assumption of hard spheres the resulting spatial arrangements are restricted by the fact that two atoms cannot come closer than half of their diameter [70, 71]. Since this model was intentionally based on monoatomic phases, it was refined by Polk et al. [72] for an adaption to metallic glasses consisting of two different elements, namely metals on the one hand and metalloids on the other hand. Further development is realized within the stereochemically defined model by Gaskell [73], assuming trigonal prisms of metal atoms around the metalloid to fill the 3D-space densely but randomly. Miracle and co-workers [44, 45, 74, 75] introduced the "Efficient Cluster Packing Model" based on a solute and solvent atom approach. Solute centered atomic clusters are formed, which are optimized to lead to a high density depending on the radius ratios of solute and solvent atom within the first coordination shell. The analytical tools used for the validation of the presented models are i.e. pair distribution function analysis [76], Voronoi tessellation methods [77], coordination number analysis or common neighbor analysis [78].

Computational analyses providing proposals for the structure of metallic glasses on the atomic scale can be verified by experimental means. Several challenges originating from the diversified, non-unique arrangements of atoms in three dimensional space have been adressed. The information extracted is mostly of statistical character of local structures and has to be revealed and analyzed in different ways in order to enable a description of atomic positioning in an accurate way. X-ray [48, 49, 79] and neutron diffraction [48, 49, 79] as well as

Introduction

X-ray absorption fine structure analysis [47, 49] provide satisfactory results on the 3D structure for multicomponent systems if multiple, element specific measurements are conducted. (Extended) X-ray absorption fine structure analysis [80] and X-ray absorption near edge structure analysis [81] are used for structural characterization employing the effect of characteristic absorption edges for each element. The results obtained thereby are transferable to diffraction measurements by giving partial, element specific pair distribution functions (see chapter 3.2 for more detailed information). Fluctuation electron microscopy [82, 83] is another technique which reveals information about the medium range order of metallic glasses. Here a highly focused X-ray beam is scanned across the sample to measure the diffracted intensity from small volumes, while the fluctuations measured stem from differences in structural arrangements and orientations of the aforementioned volumes.

1.4 PROPERTIES OF METALLIC GLASSES

The retained metallic bonding in combination with the absence of grain boundaries and dislocations impacts beneficially on the mechanical attributes of metallic glasses, positioning the elastic limit close to the theoretical strength [34], see Figure 1-2 [84]. Additionally the high compressive fracture toughness of ~57 MPa m^{½} for "Vitreloy 1" ($Zr_{41.25}Ti_{13.75}Cu_{12.5}Ni_{10}Be_{22.5}$) [85] and an elastic strain limit reaching 2% [37] paired with a higher tensile strength and Vicker's hardness [38] than measured for their crystalline counterparts underline the extraordinary properties of metallic glasses.
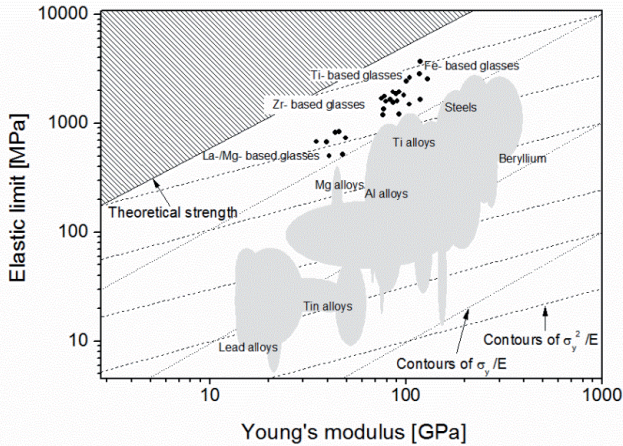
Figure 1-2:   Elastic limit σ_y as a function of Young's modulus E. The contours show the yield strain σ_y /E and the resilience σ^2_y/E. (Figure adopted from reference [84])

While some material characteristics are enhanced compared to the crystalline counterparts, the Young's modulus is generally comparable or lower (due to a lower density). A linear relationship between E and the hardness, as well as between E and the tensile fracture strength is reported for several metallic glasses [86]. The observed differences to crystals may mainly stem from different deformation and fracture mechanisms: For metallic glasses inhomogeneous plastic flow without work hardening in highly localized shear bands is observed – leading to catastrophic failure and limited plasticity [72].

Like for crystalline metallic alloys, both kinds of magnets can be found within the class of BMGs: hard and soft magnets. As a representative of hard magnetic metallic glasses, one can state the family of (Nd,Pr)-Fe based metallic glasses. They offer a high coercivity, but some of them are lacking the proof of a glass transition, while exhibiting amorphous characteristics [86]. The soft magnetic metallic glasses are mainly based on the two elements Fe and Co and are ferromagnetic due to the absence of magneto-crystalline anisotropy. Indicators for "good soft magnets" are a high saturation magnetization of up to 1.3 T, low coercivity and high effective permeability of ~20000 [87]. These guidelines are fulfilled for Fe-based systems such as the Fe-(Al,Ga)-metalloid alloy [88, 89]. $Fe_{73}Ga_4P_{11}C_5B_4Si_3$ bulk metallic glass plates reveal a permeability even reaching 110000 which can be further improved by annealing to 160000 [90]. For thin film metallic glasses in particular, film thickness dependent properties like spin reorientation transition are reported [18, 19, 40].

Introduction

1.5 CO-BASED METALLIC GLASSES

After their first reference in 1996 [88] the family of Co-based metallic glasses has widely been studied within the past years [39], because of the attractive combination of high fracture strength [39, 91] and excellent soft magnetic properties [18, 19, 40]. By modifying the alloying elements and hence improving the glass' stability, these superior characteristics can even be enhanced further [41, 92, 93]. The crystallization behavior was also subject of research [94, 95] as well as the effect of doping elements [39, 96, 97]. The outstanding role of Co-based glasses within the class of metallic glasses and compared to well established crystalline materials is shown in Figure 1-3. The fracture strength of the respective phases is plotted against their Young's modulus. The slope of the dashed lines indicates the elastic strain.
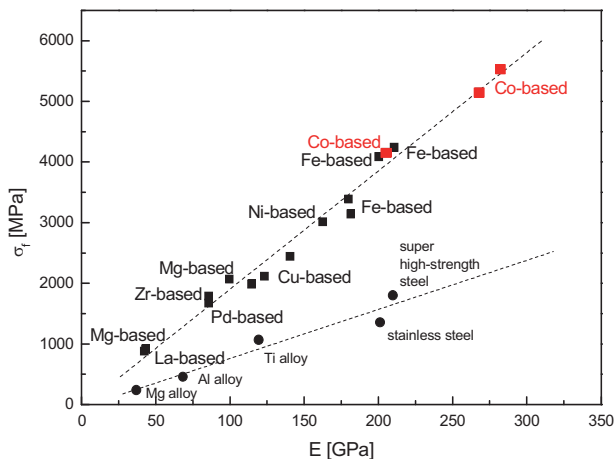
Figure 1-3:   Correlation of fracture strength and Young's modulus for several bulk metallic glasses and crystalline alloys, adopted from Ref [39].

Due to these exceptional properties much research aimed to develop suitable Co-based alloy systems and modify their compositions to tailor various material characteristics. As a result, a number of multicomponent metallic glass systems have been reported, such as Co-Fe-B-Si [98], (Co-Fe)-(Nb,Zr)-(B,Si) [92, 94-97, 99, 100], Co-Fe-(Ta,Mo)-(B,Si) [18, 19, 39-41, 91] and (Co,Fe,Ni)-(Zr,Hf,Nb,Ta,Mo,W)-B [93]. The materials properties investigated cover a wide range from glass forming ability [99-101] over thermal stability to strength [39, 41, 91, 99] and

magnetic properties [18, 19, 40, 92, 93, 97, 98, 100, 101]. The here reported systems all follow the general constitution (Co,Fe)-(transition metal)-(B,Si).

Co-based glasses possess a unique local atomic configuration, similar to the related Fe-based amorphous alloys Fe-Nb-(Ta)-B for which a network-like structure is indicated based upon coordination number and atomic distances analysis [39, 65, 102]. This spatial arrangement of atoms leads to the precipitation of a $(Fe,M)_{23}B_6$ (M=Nb,Ta) phase consisting of distorted trigonal prisms formed by Fe-B interconnections through bridge atoms of Nb or Ta. Similar mechanisms are expected for Co-based glasses, due to analogies in alloy components and primary crystallization phases. For Co-based glasses the precipitation of the metastable face-centered cubic phase $(Co,Fe)_{21}Ta_2B_6$ was reported, which is an isomorph of $(Fe,M)_{23}B_6$. [39, 91, 103] The formation of this large and complex cell implies long-range atomic rearrangements and hence leads to a high resistivity against crystallization as well as to the aforementioned high strength.

Computational studies on Co-based metallic glasses are rare. Kaban et al. [49] studied the atomic structure of $Co_{43}Fe_{20}Ta_{5.5}B_{31.5}$ metallic glass and its effect onto glass-forming ability and thermal stability by X-ray diffraction and absorption experiments as well as by reverse Monte Carlo modeling. The study on Co-Fe-Ta-B metallic glass [104] and its elastic and magnetic properties, carried out within the framework of this thesis, was one of the first a priori based investigations for Co-based glasses [105]. A few studies on associated systems based on magnetic elements like Fe [61, 62, 66, 106] have been published. Systematic *ab-initio* studies on the effect of element substitution are rare, e.g. the work done by He et al. [107], and have not been reported for Co-based glasses.

1.5.1 CO-FE-TA-B

The glassy alloy $Co_{43}Fe_{20}Ta_{5.5}B_{31.5}$ in particular not only exhibits the best glass-forming ability within the family of Co-based metallic glasses [41], but it also shows an extraordinary high fracture strength of 5185 MPa [39, 91, 103] (higher than any other bulk crystalline and amorphous material [41, 91]). This strength is attributed to the strong bonding nature, the network-like structure as well as to the large negative values for enthalpies of mixing (and hence a high density) within the constituent elements [41, 91, 103]. Furthermore a Young's modulus of 268 GPa [39, 91, 103], a tensile strain of 1400% in the supercooled liquid region [103] and an increased T_g/T_l (indicating an enhanced glass forming ability) upon alloying with Mo and Si were reported [41]. Excellent soft magnetic properties have also been measured: An extremely high permeability of 550000 [91] and a

tailorable spin reorientation transition with the Curie temperature up to 450 K [18, 19, 40] can be found in literature. Experiments on the corrosion properties show passivity in NaCl, HCl and H_2SO_4 with corrosion rates in the order of 10^{-3} mm/year [108]. This combination of properties enables the application of $Co_{43}Fe_{20}Ta_{5.5}B_{31.5}$ as structural as well as magnetic material. Potential applications as magnetic material are magnetic head cores, thin film inductors, transformer cores as well as quick-response magnetic sensors [18, 19, 34, 39, 40, 91] while a structural application may be the use $Co_{43}Fe_{20}Ta_{5.5}B_{31.5}$ thin films in combination with $L1_0$ FePt(111) in form of a bilayered structure for patterned media [25].

Although there are investigations on the effect of transition metal addition or replacement for example on fracture strength for the Co-Fe-Ta-B glassy alloy [41], the impact of the metalloid element in particular seems to be wide ranging. The presence and population of the metalloid alloying elements, chiefly B and Si, define the properties of Co-based metallic glasses: They stabilize the supercooled liquid region [41, 93, 99-101], they facilitate a network like structure enabling high strength [101] and they act beneficially on the magnetic properties of the respective alloy by influencing the saturation magnetization, coercive forces and effective permeabilities [100, 101]. An increase in valence electron concentration, size or electronegativity of the metalloid element is expected to impact the overall properties. Namely, it is reported that a high average difference in electronegativity among the elements leads to a high glass-forming ability [109]. Constitution of an optional ratio of both elements, B and Si, tunes the aforementioned properties of Co-based metallic glasses [100, 101]. Nevertheless, the content of Si in Co-based bulk metallic glasses is usually limited to a few atomic percent due to restrictions in glass forming ability. While an investigation on the impact of Si substitution of B in Co-Fe-Ta-B (employing the efficient quenching rates of physical vapor deposition) was reported [110], P and/or S substitutions of B have not yet been considered experimentally, although P is reported to increase the critical thickness (if substituted for 2 at.% B) and the glass-forming ability within the Fe-based systems $Fe_{78}Si_9B_{13}$ [111] and $Fe_{68.3}C_{6.9}Si_{2.5}B_{6.7}P_{8.8}Cr_{2.2}Mo_{2.5}Al_{2.1}$ [112].

1.6 OUTLINE OF THE THESIS

Within the framework of this thesis the generation, validation and implementation of a first principles model for Co-Fe-Ta-X (X=B,Si,P,S) metallic glasses is described. Composition induced changes in short range order, charge transfer and bonding nature are correlated with materials properties such as density, elasticity and magnetism.

Synthesis of Co-Fe-Ta-(B/Si) thin film metallic glasses by combinatorial magnetron sputtering allows for the experimental validation of the *ab-initio* model in terms of pair distribution function, density, elasticity and magnetization values. Consistency with literature data of bulk $Co_{43}Fe_{20}Ta_{5.5}B_{31.5}$ metallic glasses [103] is also obtained. The results for the Co-Fe-Ta-B system can be found in chapter 4.2, while the results for the Si containing glass are presented in chapter 4.3. Implementation of the generated model allows for a systematic study of the effect of valence electron concentration and size of the X element in $Co_{43}Fe_{20}Ta_{5.5}X_{31.5}$ (X=B,Si,P,S) on the aforementioned properties and is presented in chapter 4.4.

This systematic *ab-initio* based study on the structure-elasticity-electronic structure correlation for $Co_{43}Fe_{20}Ta_{5.5}X_{31.5}$ (X=B,Si,P,S) enables the identification of composition induced changes in short range order, charge transfer and bonding nature as well as their correlation with materials properties such as density, elasticity and magnetism. Based on this knowledge future design strategies for metallic glasses may be derived.

2 THEORETICAL METHODS

The development of quantum mechanics within the last century and the fact that it accurately describes matter fundamentally enabled materials scientists to investigate properties on the atomic and electronic scale. The employment of computational simulations based on density functional theory allows for the validation of models drafted and to gain information which is not accessible by experiments. While defining the required atomic positions within a crystal is straight forward, it is more challenging in the case of liquid or amorphous materials. Nevertheless, DFT is a promising tool to examine these disordered phases. Metallic glasses have been investigated regarding the effect of (optimized) composition on atomic structure and glass forming ability [56-59, 113, 114]. Other fields of interest for computationally based research on metallic glasses are composition dependent dynamic properties [114] or the effect of valence electron concentration on the glass transition temperature [60]. The work on Co-Fe-Ta-B and its elastic and magnetic properties [104] presented here is one of the first a priori based investigations for Co-based glasses [105].

The mathematical implementation of the quantum behavior of atoms is the Schrödinger equation, with DFT as a successful approach to find a solution for it. The main fruits one can reap out of this computational material research are: cohesive energies (phase stability), ground state properties, electron density distributions ((partial) density of states), charge states of atoms or the chemical bonding of the constituent elements. Nowadays the models employed to gain these characteristics are normally limited to ~100 atoms due to the fact that the CPU requirements rise with the power of three as the number of electrons increases. See chapters 1.3 and 4.1 accordingly.

The simple, time-independent Schrödinger equation

$$H\psi = \epsilon\psi,$$

Equation 2-1

contains the necessary physics to describe real materials, but interactions between multiple electrons and nuclei need to be explicitly accounted for. Hence the Schrödinger equation becomes more complex, evolving towards a many body system. The approximation established by Born and Oppenheimer [115] reduces this complexity: Since atoms consist of (heavy) nuclei and (light) electrons, electrons will react much faster to changes. While the nuclei are kept fixed, the

Theoretical Methods

equations that describe the electron motion are solved and will thus enable the ground state energy determination.

$$\left[-\frac{\hbar^2}{2m} \sum_{i=1}^{N} \nabla_i^2 + \sum_{i=1}^{N} V(\boldsymbol{r}_i) + \sum_{i=1}^{N} \sum_{j<i} U(\boldsymbol{r}_i, \boldsymbol{r}_j) \right] \psi = \Theta \psi$$

Equation 2-2

Within Equation 2-2 the electron mass, kinetic energy of each electron, interaction energy between each electron and collection of atomic nuclei as well as the interaction energy between different electrons are also taken into account [116]. The methodology of DFT correlates this ground state energy with the ground state electron density and is based on two fundamental mathematical theorems by Hohenberg and Kohn [117] as well as subsequently formulated equations by Kohn and Sham [118]. Their first theorem states that the ground state energy can be expressed as a functional of the electron density, while the second one contains the conclusion that the ground state energy minimizes the total energy of the system. So a system is fully determined by its electron density. The advantage of the aforementioned equations by Kohn and Sham is that they are single-electron wave functions that only contain of three terms:

$$\left[-\frac{\hbar^2}{2m} \sum_{i=1}^{N} \nabla_i^2 + V(\boldsymbol{r}) + V_H(\boldsymbol{r}) + V_{XC}(\boldsymbol{r}) \right] \psi_i(\boldsymbol{r}) = \varepsilon_i \psi_i(\boldsymbol{r})$$

Equation 2-3

To solve these equations, the exchange-correlation functional has to be specified. As the true form is not known, approximations have to be employed: Assuming an ideal, uniform electron gas with non-interacting particles, the respective electron density will be uniform and constant in the 3D space, too, so the exchange correlation potential can be set to the exchange correlation potential of the Fermi gas. Since this approximation only uses the local density to define the quested term, it is called LDA (local density approximation) [119]. Another often used approximation further takes the gradient of the electron density into account: GGA (general gradient approximation). The ways to describe the gradient vary from GGA functionals to GGA functionals. One of the most used functional is the Perdew-Wang functional (PW91) [120] as used within this thesis. To minimize computational resources needed for DFT calculations, another approximation is made: Pseudopotentials replace the electron density of less relevant core electrons by a smoothed density. If these potential are denoted as hard, soft or

ultrasoft depends on the minimum cutoff energy limit set by these potentials ranging from high to low, respectively. *Ab-initio* molecular dynamics allows for the atoms to move within a real material since there are several topics where the properties of interest are a function of former atomic positions. One field is, as mentioned before, the field of non-crystalline solids - metallic glasses as within this thesis-, where an amorphous state has to be created prior to the computational analysis of static configurations.

2.1 COMPUTATIONAL DETAILS

Within this thesis two different codes were employed: the Vienna Ab Initio Simulation Package (VASP) [121] and the Open source package for Materials Explorer (OpenMX) [122, 123].

2.1.1 MOLECULAR DYNAMICS

Ab-initio molecular dynamics, as implemented in the OpenMX code [122, 123], with generalized gradient approximation and linear combination of pseudoatomic orbitals [124], was used to model Co-Fe-Ta-X (X=B,Si,P,S) metallic glasses. The following basis functions were applied: Co5.5-s2p1d1, Fe5.0-s1p2d1, Ta7.0-s2p1d1f1, B4.5-s2p2, Si5.0-s2p1, P6.0-s2p1d1 and S6.0-s2p2d1. The first symbol and number designate the chemical name and confinement radius, respectively, followed by the description of orbitals used.

To identify a suitable glass model describing this alloy, three different initial configurations of $Co_{43}Fe_{20}Ta_{5.5}B_{31.5}$, based on stoichiometric bcc supercells with Co, Fe, Ta and B on *ad hoc* random positions, were evaluated. Boron was placed either on (i) substitutional sites (128 atoms), (ii) substitutional sites with 5% larger lattice parameter (128 atoms) or (iii) substitutional sites, including 10% randomly introduced vacancies independent of atomic species (115 atoms). All initial configurations were held at a temperature of 4000 K by scaling the velocities for 400 fs and were then quenched to 0 K. Initially the density of all configurations was set to be identical. At 0 K all configurations were relaxed in terms of atomic positions and volumes and treated as ferromagnetic. For configuration (iii), containing 115 atoms, the applied cooling rates to 0 K were infinite, $1x10^{16}$ and $1x10^{14}$ K/s. As the cooling rate during sputtering are estimated to be beyond 10^{10} K/s, reaching 10^{15} K/s [125], the here studied cooling rates are relevant for the sputtering experiments conducted.

As for the B containing cell, all other configurations containing Si, P and S were held at a temperature of 4000 K for 400 fs by scaling the velocities and were then

Theoretical Methods

quenched to 0 K, simulating an infinite cooling rate. At 0 K all configurations were relaxed in terms of atomic positions and volumes. The force convergence criterion was set to 0.51 eV Å^{-1}.

2.1.2 STATICS

All static calculations, including the extraction of total and partial DOS as well as bonding analysis were conducted employing the Vienna Ab Initio Simulation Package (VASP) [121] which is also DFT based [52]. The applied parameters for the VASP calculations were as follows: generalized-gradient approximation (Perdew-Wang 91) exchange-correlation functionals [120] with Vosko-Wilk-Nusair [126] spin interpolation, based on ultrasoft pseudopotentials [124]. A Brillouin zone on a 3x3x3 Monkhorst-Pack grid [127], centered at the Γ-point, as well as an energy cutoff of 500 eV were applied. Furthermore an electron smearing of 0.2 eV based on the tetrahedron method with Blöchl corrections [54, 128] and a convergence criterion of 0.01 meV for the total energy was set. All calculations were carried out at 0 K. Cohesive energies are defined as negative values. The bulk moduli were obtained by the uniform compression approach and fitting the energy-volume curves to the Birch-Murnaghan equation of states [129]. The effective charge of an element is defined within this study as the charge difference of a neutral atom in comparison to the present charge state within the alloy [130]. The charge was deduced by the Bader charge analysis [131] as implemented in the program written by Henkelman and co-workers [132, 133] by dividing the electron density distribution along surfaces implying a gradient of zero along the surface normal. Convergency was tested by calculating the charge with a series of variable grids.

3 Experimental Methods

3.1 Thin Film Deposition

Physical vapor deposition is a valuable synthesis route for metallic glasses [21-24, 134]: Due to efficient quenching of surface-diffusion controlled phase formation the generation of metastable phases is enabled [135, 136] and unprecedented high cooling rates are reached [125]. Magnetron sputtering, as one sub-category of the PVD processes, will be described in more detail below.

The concept of sputtering implies material ejection upon impulse transfer after bombardment with high-energy ions. These high energy ions originate from the sputter gas, which is in the fourth state of matter: plasma. As sputter gas a noble gas is chosen unless reactive film deposition is intended. In this case, reactive gases (e.g. O_2, N_2, C_2H_2) are used. The sputtering gas is introduced to the deposition chamber after high (10^{-3} to 10^{-7} mbar) or ultra-high vacuum (below 10^{-7} mbar) is obtained. Plasma is generated and sustained by an electric field and fills the space between cathode (target) and anode (substrate and chamber walls). If accelerated positive gas ions interact with the target surface, energy is transferred to the surface atoms and diminished by further collisions in the inner regions of the target. If the transferred energy is larger than the surface binding energy, atoms or molecules are sputtered. In addition to the sputtering effect secondary electrons are generated which may subsequently collide/scatter and ionize further noble gas atoms and will hence support the perpetuation of the glow discharge. The movement of sputtered species is governed by a line-of-sight-characteristic, which means that primarily the area facing towards the cathode will be deposited with target material. Atoms or molecules reaching the substrate will be physisorbed, followed by diffusion processes and chemisorption and finally result in a continuous layer. In order to deposit amorphous films, the adatom mobility has to be kept minimal and thus the energy supplied to substrate and growing layer. One key factor defining substrate conditions is the supplied energy, for example heat, so intentional heating is disadvantageous and rather cooling (e.g. by liquid nitrogen) should be considered. Another way to control the energy of the arriving particles and hence to the growing layer, is a distinct working gas pressure or the application of substrate bias.

A "magnetron" cathode consists of magnets placed behind the target creating a magnetic field (see Figure 3-1 for a simplified scheme of a magnetron sputtering setup).

Experimental Methods
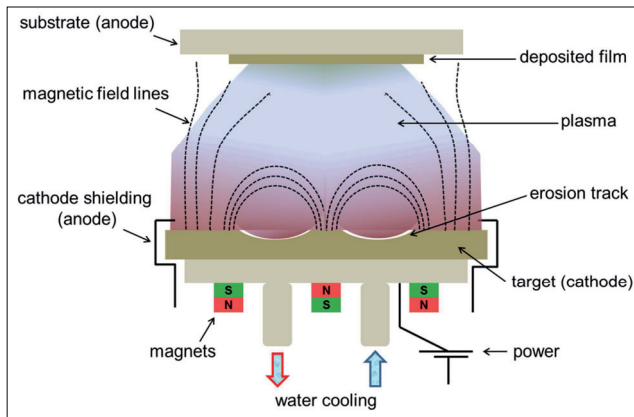
Figure 3-1: Simplified scheme of a planar magnetron sputtering setup.

This traps secondary electrons close to the target surface and hence increases the degree of ionization of the sputter gas. A higher plasma density is achieved resulting in higher sputtering rates at lower power compared to conventional sputtering. Today almost all sputter depositions are carried out with the help of magnetrons. For conductive target materials, a direct current (DC) is used, while for non-conductive targets like B, as used in this work, radio frequency (RF) needs to be employed. For RF the alternating polarization of the current prevents the target from charging. In this case the sign of the anode-cathode bias is varied at a high rate.

3.1.1 EXPERIMENTAL SETUP

To evaluate the *ab-initio* molecular dynamics model, Co-Fe-Ta-(B/Si) thin films were deposited in a UHV-deposition system with a base pressure of 10^{-8} mbar. A combinatorial physical vapor deposition strategy was employed [137] based on co-sputtering of Co, Fe, Ta (each with a purity of 99.95%) and B (99.5% purity) or Si (99.99999% purity) targets. All elemental targets were 2" in diameter and mounted on magnetrons in an off-axis setup (the angle between substrate normal and plasma source is fixed to 19°; see Figure 3-2 for a schematic drawing).
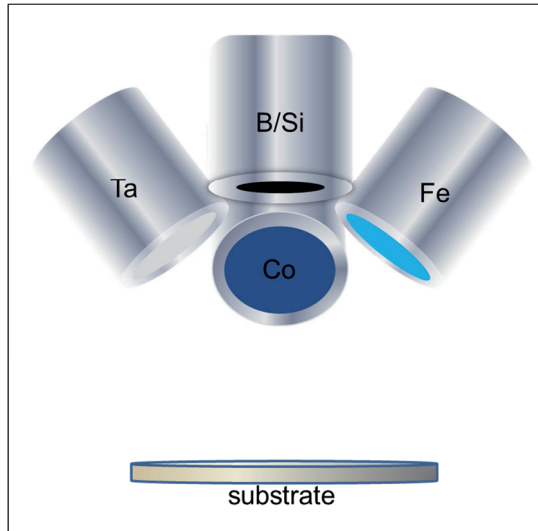
Figure 3-2:   Schematic deposition setup for the combinatorial Co-Fe-Ta-B/Si metallic glass thin film synthesis.

For Co, Fe, Ta and Si targets DC sputtering was utilized, for B a RF generator was employed. The power densities were 1.1-1.2, 0.6, 0.2-0.3, 8.4 and 1.7 W/cm^2 for Co, Fe, Ta, B and Si respectively. For Ta a shutter, blocking $\sim$2/3 of the target area, to decrease the Ta flux contributing to film growth, was installed. This setup is attributed to the fact that neither a further increase of RF power for B nor a further decrease in DC power for Ta was feasible with the equipment in hand. All power densities were determined to ensure a composition comparable to the one reported for the BMG $Co_{43}Fe_{20}Ta_{5.5}B_{31.5}$ [103] in the center of the sample. The argon pressure of $4x10^{-3}$ mbar was kept constant during sputtering. Electrically grounded Si (100)-wafers were used as substrates, which were neither rotated nor intentionally heated. The target to substrate distance was $\sim$10 cm which results in a deposition rate of $\sim$7 nm/min for the Co-Fe-Ta-B glass and $\sim$8 nm/min for the glass containing Si.

3.2 THIN FILM ANALYSIS

The thin films deposited within the framework of this thesis were analyzed in terms of composition, structure, density, stiffness and magnetization using atom probe tomography, X-ray diffraction, X-ray reflectivity, nanoindentation and a superconducting quantum interference device, respectively. The different

Experimental Methods

methods will be introduced shortly within this chapter accompanied by the respective measurement parameters used.

The challenge to enable both, the determination of atomic positions within the 3D space and their chemical identity lead to many improvements and developments within the microscopy community. Currently, atom probe tomography is the only one technique offering both simultaneously [138]. Within an APT measurement hundreds of millions of atoms are imaged, originating from a sharp needle shaped specimen. The method itself is destructive in nature: The respective surface atoms are extracted from a cooled needle tip by means of field evaporation or laser pulsing and are projected as ions onto an imaging screen (see Figure 3-3). The coupling of position determination and chemical identification is realized by the employment of position sensitive detector in combination with a time-of-flight mass-over-charge-ratio measurement. The high analytical sensitivity at the order of 10 atomic parts per million is combined with atomic scale resolution (~0.2 nm depth resolution and 0.4 nm lateral resolution) [139].
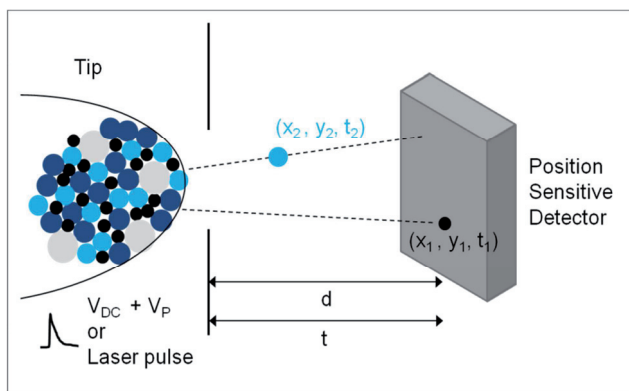
Figure 3-3: Simplified scheme of a 3D atom probe tomography setup.

The thin film compositions in the center of the samples were determined with a LEAP 3000X HR atom probe with a laser energy of 0.20-0.3 nJ, a detection rate of 1.0-2.0%, base temperature of 30-60 K and a pulse rate of 250 kHz as well as in a LAWATAP system with a sample temperature of 40-50 K, using laser pulsing mode, UV irradiation and detection rates of 0.01-0.05 ions/pulse.

X-ray diffraction is a widespread, non-destructive method employed to gain structural information of the materials under study. In case of crystalline samples XRD allows for crystal structure and phase identification, as well as to extract

information on grain sizes or internal strain. Either constructive or destructive interference of X-rays with periodically arranged atoms on lattice planes is detected. If the diffracted beam intensity is plotted versus diffraction angle, a unique diffraction pattern is obtained depending on the present structure of the sample. In case of crystallinity the detected intensity of diffracted beams will vary depending on the interplanar lattice spacings, according to Bragg's law:

$$n \cdot \lambda = 2 \cdot d \cdot \sin \Theta$$

Equation 3-1

For amorphous materials no characteristic peaks within the diffractogram can be observed since long range order causing constructive interference is absent. Instead, amorphous samples show a broad hump at $2\theta < 50°$ originating from short range order, while long range order is missing. Figure 3-4 shows the comparison of XRD scans obtained from amorphous, as-deposited Co-Fe-Ta-B metallic glass (exemplarily for this work) and the same system after annealing at 1050°C. Well defined characteristic peaks, of a crystalline material, are clearly recognizable in the annealed samples, whereas the as-deposited sample shows typical amorphous features (broad "hump" between 40-50°).
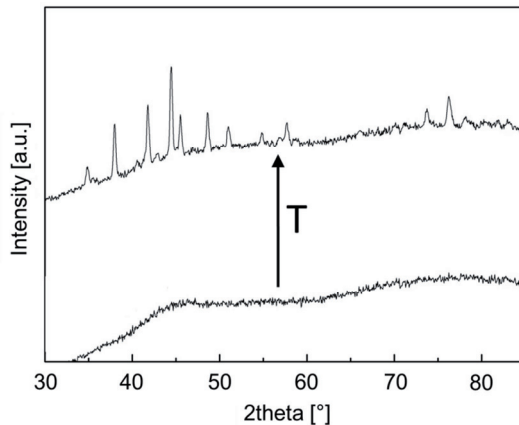
Figure 3-4: X-ray diffractogram showing the Co-Fe-Ta-B metallic glass in the amorphous, as deposited state (lower curve) and in the crystallized from after heat treatment at 1050°C.

The structure of the deposited films was determined using a grazing incidence X-ray diffractometer (Bruker AXS D8 Discover General Area Detection Diffraction System). A collimator with a diameter of 0.5 mm and an incidence angle of 15° as

Experimental Methods

well as Cu K$_\alpha$ irradiation and the setting of 40 mA/40 kV generator voltage were used.

The absence of well-defined peaks poses a serious challenge to the structural evaluation of amorphous samples. Further analysis has to be done to gain insight into the inherent atomic arrangements of the glassy material. High energy photons within the X-ray diffraction technique allow for better quality structural analysis of metallic glasses by pair distribution functions compared to standard laboratory XRD techniques.

A (partial) pair distribution function is a measure for the probability to find (element specific) atoms in a certain distance from an average (element specific) center atom. For a crystalline material this function would outline as sharp peaks at defined distances. In the case of metallic glasses the shell like structure with the fading out at higher distances is represented by a pronounced first peak, followed by a minor second peak and a subsequent broad region. Figure 3-5 shows this phenomenon exemplarily for a GeSbTe alloy [140].
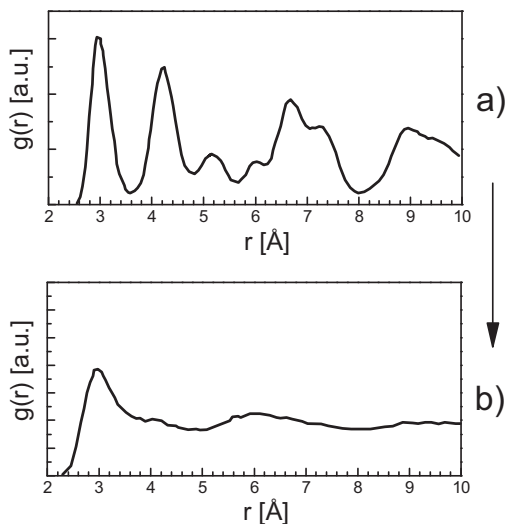
Figure 3-5:   Pair distribution function for GST at temperatures of a) 600 K and b) 2000K. The loss of long range order towards the amorphous/liquid character is clearly seen. Data adopted from Ref [140].

PDFs are employed to analyze local structures and can be experimentally obtained by a Fourier transformation of the structure factor gained by X-ray or

neutron diffraction measurements. While the experimentally obtained PDFs lack the ability to reconstruct the 3D space upon a degenerate 2D signal and hence require multiple element specific measurements to solve all the partials, PDFs stemming from computational models provide partial pair distribution functions directly.

The total structural factor $S(q)$ is obtained from the normalized elastically scattered intensity, $I_e(q)$ [76]

$$S(q) = 1 + \frac{I_e(q) - [\sum_{i=1}^{n} c_i \, f_i^2(q)]}{[\sum_{i=1}^{n} c_i f_i(q)]^2}$$

Equation 3-2

where c_i and $f_i(q)$ are the atomic concentrations and scattering factors of the atomic species of type i (i =Co, Fe, Ta, B), respectively. The corresponding reduced pair distribution function, $G(r)$, can be obtained through a sine Fourier transformation:

$$G(r) = 4\pi r[\rho(r) - \rho_0] = \frac{2}{\pi} \int_{0}^{q_{max}} q(S(q) - 1) \sin(rq) \, dq$$

Equation 3-3

From $G(r)$ the PDF, $g(r)$ can be calculated by:

$$g(r) = \frac{\rho(r)}{\rho_0} = \frac{G(r)}{4\pi\rho_0 r} + 1$$

Equation 3-4

A PDF, $g(r)$, can also be calculated from the structural model like the one presented in this thesis, using the relation

$$g(r) = \frac{1}{4\pi\rho_0 r^2} \sum_i \sum_j \frac{b_i b_j}{\langle b \rangle^2} \delta(r - r_{ij})$$

Equation 3-5

where the sum goes over all pairs of atoms i and j within the model separated by r_{ij}. In this way, the arrangement and symmetry of the first coordination shell can be described.

Experimental Methods

The integration of the first peak gives the total coordination number which in turn describes the quantity of atoms in the first coordination (neighbor) shell. Furthermore, by extracting coordination numbers for a selected center atom, indications on the bonding nature and the magnitude of dense packing can be obtained.

Pair distribution functions for the thin films studied in this thesis were extracted from X-ray diffraction experiments using high-energy photons with the BW5 wiggler beamline of DORIS III positron storage ring, DESY/HASYLAB. Ten independent scans at room temperature were acquired in transmission mode with 100 keV (λ = 0.01239 nm), 10 s illumination time, a fast image plate detector and a detector to sample distance of 51.3 cm for a high-q range cover of up to 18.5 Å^{-1}. Two-dimensional XRD patterns were integrated to the q-space using the software package FIT2D [141]. The data were then converted to the total structure factor, $S(q)$, using standard procedures described elsewhere [76]. The integrated data were corrected for sample absorption, fluorescence contribution and inelastic (Compton) scattering.

The X-ray reflectivity technique allows for a surface sensitive analysis of surfaces, thin films and multilayers [142]. The basic principle of XRR is the reflection of an X-ray beam on a flat surface at very low incidence angles. The critical angle at which the reflected beam becomes partially absorbed, is a measure for the density of the investigated material. In the case of thin films or multilayers the film thickness, reflected in periodic intensity variations, can be derived as well. Due to the imperfectness of an existing interface the reflected intensity will deviate from the perfect one, predicted by the law of Fresnel reflectivity [143]. This deviation is employed to extract a density profile of the interface normal to the surface. An approximation of the X-ray reflectivity of a real interface with an average density profile $\rho_e(z)$ is given by Equation 3-6 [144]:

$$\frac{R(Q)}{R_F(Q)} = \left| \frac{1}{\rho_\infty} \int\limits_{-\infty}^{\infty} e^{iQz} \left(\frac{d\rho_e}{dz} \right) dz \right|^2$$

Equation 3-6

with Q=4πsin(θ)/λ.

The comparison of the measured reflectivity with parameterized models and subsequent fitting by parameter variation until the experimental curve matches the theoretical one gives the density of the layer of interest.

X-ray reflectivity measurements were carried out with a Philips PW1820 diffractometer using Cu K$_\alpha$ radiation and subsequent fitting of the experimental curves using the GenX software [145].

One way to measure the mechanical properties of materials is to indent the sample with controlled force and record the response of the material. This technique is called nanoindentation. When the diamond tip penetrates the sample with increasing force and is subsequently withdrawn, a loading-unloading curve can be recorded (see Figure 3-6).
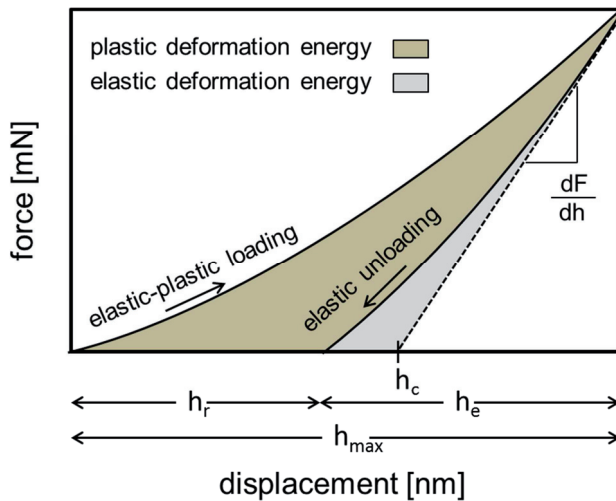
Figure 3-6: Schematic load-displacement curve obtained from nanoindentation showing elastic and plastic contributions.

The curve shown in Figure 3-6 allows for stiffness and hardness determination. The elastic modulus is defined as the ratio of stress to strain for a one-directional acting tensile stress. The slope of the initial unloading curve is indicative for the stiffness S (corresponding to the method introduced by Oliver and Pharr [146], assuming that no plastic deformation occurred). This contact stiffness can be further used to obtain the reduced Young's modulus:

$$E_r = \frac{1}{\beta} \frac{\sqrt{\pi}}{2} \frac{S}{\sqrt{A_p(h_c)}}$$

Equation 3-7

Experimental Methods

Here β stands for geometrical constant, $A_p(h_c)$ designates the projected indentation area and h_c is the contact depth. A tip area function correlates depth changes with the indentation size and is determined using a standard material (typically fused silica) prior to the sample measurement. To determine the Young's modulus from the reduced Young's modulus of the sample, properties of the indenter tip have to be known:

$$\frac{1}{E_r} = \frac{(1 - v_i^2)}{E_i} + \frac{(1 - v_s^2)}{E_s}$$

Equation 3-8

v_i and E_i are the Poisson's ratio and Young's modulus of the diamond indenter tip (both are known), while v_s and E_s denote the specimens properties.

For isotropic materials like metallic glasses, E is insensitive to the direction of load, for most crystalline materials it is different in different crystallographic directions. When analyzing thin films by nanoindentation it is important to assure an appropriate film thickness. A rule of thumb says that the penetration depth should be maximum 10% of the deposited film thickness. Otherwise the results will be influenced by the mechanical properties of the substrate [147].

The thin film stiffness was measured using a depth-sensing nanoindenter (Hysitron TriboIndenterTM) attached with a Berkovich indenter tip. For each measurement 18 indentations were carried out. The loads were varied between 800 and 2500 mN, which correspond to a contact depth of < 10% of the films thickness. Fused silica and sapphire were employed for tip calibration according to the method of Oliver and Pharr [146].

One way to measure extremely weak magnetic fields is the superconducting quantum interference device. This method is capable of measuring changes in a magnetic field with such sensitivity that a direct contact of analytical tool and sample is not necessary. The general assembly consists of superconducting loops and one or more Josephson junctions. These junctions in turn are built of two superconductors which are separated by a thin insulating layer. The thickness of this layer is capped to a value where electron tunneling is still possible. To maintain the necessary superconductivity, the SQUID device needs to be operated under constant cooling by liquid helium. There are two main types of SQUIDs: DC and RF SQUIDs. While an RF SQUID is made of one Josephson junction, the more sensitive DC SQUID contains of two Josephson junctions employed in parallel. The latter one is employed within this thesis. If a sample is moved through a system of superconducting detection coils (connected to a SQUID via superconducting

wires), the magnetic moment of the sample will induce a current within these coils (see Figure 3-7).
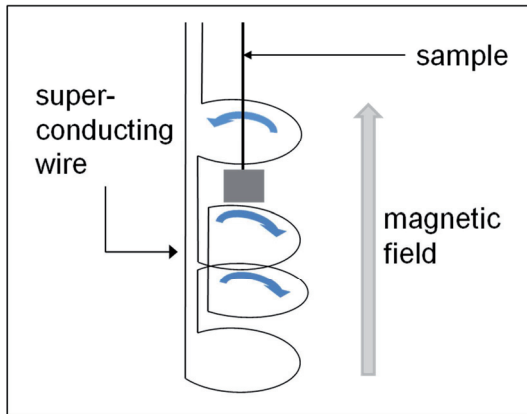
Figure 3-7:   Schematic configuration of superconducting detection coils, sample and superconducting connection wires within a magnetic property measurement system.

Since detection coils, superconducting connection wires and the SQUID input coils build a closed superconducting loop, a change in magnetic flux within the detection coils will induce a change in the persistent current in the detection coils. This current is proportional to the change in magnetic flux. The current variations in turn produce variations in the SQUID output voltage which is finally proportional to the magnetic moment of the sample.

The magnetization measurements within this thesis were performed using a Quantum Design "Magnetic Property Measurement System (MPMS®)", in DC mode. The Reciprocating Sample Option (RSO) was employed resulting in a DC magnetization absolute sensitivity of $1x10^{-8}$ emu at 2500 Oe. The samples were cut into small pieces and mounted on paper stripes using GE varnish. After varnish drying the stripes were mounted inside plastic straws to be suitable for the SQUID sample holder. Hysteresis loops were recorded at 10 and 300 K. In this way, saturation fields and magnetization were determined. For thin film measurements, signal correction is needed due to a diamagnetic signal arising from the Si substrate. So a linear curve is subtracted from the raw data, while the slope of this line is determined by points in the hysteresis loop well after reaching the magnetic saturation of the samples and extending towards higher applied fields.

4 RESULTS AND DISCUSSION

4.1 GENERATION OF THE MODEL

The discussion of a suitable configuration to describe the quaternary metallic glass system under study here is based on the total energy of each supercell. The quantitative deviation in total energy for all configurations with reference to configuration (iii) can be found in Table 4-1. It is shown here that the initial configuration (iii), containing vacancies, results in a 43 and 2 meV/atom lower total energy than for configuration (i) and (ii), respectively. This corresponds to a relative deviation of +0.6% and +0.03%, respectively. It appears that the bcc supercell vacancies provide pathways for diffusion. The total energy differences between configuration (iii) with infinite cooling and two different cooling rates differ by -34 and -93 meV/atom or -0.5% and -1.2%, respectively. Thus, the total energy of configuration (iii) does not significantly depend on the cooling rate. Based on the total energy analysis and CPU requirements, configuration (iii) with an infinite cooling rate was selected as the suitable description of the $Co_{43}Fe_{20}Ta_{5.5}B_{31.5}$ metallic glass.

		configuration				
		(i)	(ii)	(iii)		
	cooling rate	infinitely	infinitely	infinitely	1×10^{16} K/s	1×10^{14} K/s
ΔU_{tot} [meV/atom]		43	2	0	-34	-93

Table 4-1: *Relative deviation in total energy (U_{tot}) of all probed configurations as obtained within the ab-initio study for $Co_{43}Fe_{20}Ta_{5.5}B_{31.5}$ with reference to configuration (iii), infinitely cooling rate*

Figure 4-1 shows exemplarily the initial and final configuration (iii) for $Co_{43}Fe_{20}Ta_{5.5}B_{31.5}$. No evidence for long range ordering and formation of segregations can be seen. Hence this final configuration appears to be amorphous.

Results and Discussion
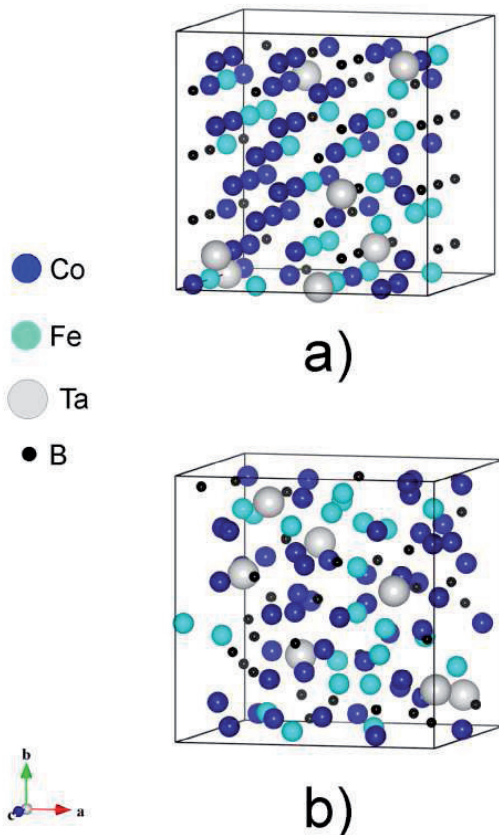
Figure 4-1:   Configuration (iii) for $Co_{43}Fe_{20}Ta_{5.5}B_{31.5}$: (a) initial state and (b) after relaxation.

4.2 EXPERIMENTAL VALIDATION: CO-FE-TA-B

In this chapter, the model to study the correlation between the elastic properties of Co-Fe-Ta-B metallic glasses and the electronic structure thereof is established and validated. The validation is achieved by experimental replication of the pair distribution function, density and elasticity.

4.2.1 DENSITY

The structure of the deposited film was determined to be X-ray amorphous with a broad hump around two theta of 44-45° (see Figure 3-4 in chapter 3.2). While the composition for the *ab-initio* study was $Co_{43}Fe_{20}Ta_{5.5}B_{31.5}$, the thin film

composition in the center of the sample was determined based on the atom probe data to be $Co_{45.5}Fe_{24}Ta_6B_{24.5}$. Hence an additional simulation with this experimentally obtained composition was conducted, keeping all other parameters constant to quantify the effect of a reduction in B concentration by 7 at% on the stiffness and density.

Density values were derived from *ab-initio* molecular dynamics and X-ray reflectivity measurements. The theoretical densities obtained from energy-volume curves are 8.19 g/cm^3 for $Co_{43}Fe_{20}Ta_{5.5}B_{31.5}$ and 8.42 g/cm^3 for $Co_{45.5}Fe_{24}Ta_6B_{24.5}$. XRR shows that the density of the deposited film is ~8.80 g/cm^3. The theoretically obtained densities listed in Table 4-2 and shown in Figure 4-2 for $Co_{43}Fe_{20}Ta_{5.5}B_{31.5}$ and $Co_{45.5}Fe_{24}Ta_6B_{24.5}$ are in good agreement to the reported value for $Co_{43}Fe_{20}Ta_{5.5}B_{31.5}$ bulk metallic glasses with 8.65 g/cm^3 [103] showing a deviation of 5% and 3%, respectively. The thin film value measured in this study differs to the previously reported bulk value [103] by only 2%; the deviations to the theoretical results of $Co_{45.5}Fe_{24}Ta_6B_{24.5}$ and $Co_{43}Fe_{20}Ta_{5.5}B_{31.5}$ are 5% and 7%, respectively, indicating a weak dependence on the chemical composition in the here studied range. Based on the good agreement between calculated, previously reported and here measured thin film density it can be learned that the here established computational methodology is useful to describe the density of Co-Fe-Ta-B metallic glasses.
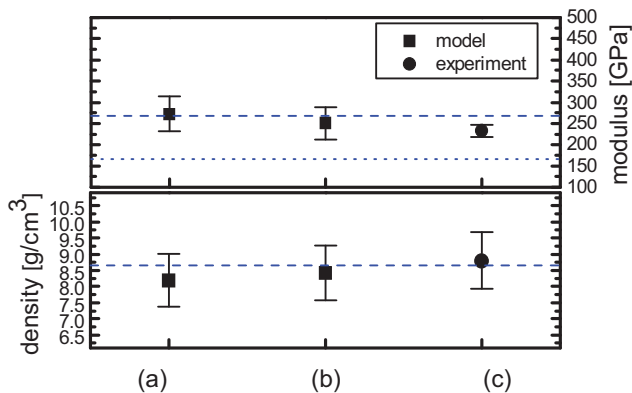
Figure 4-2: Obtained results for moduli and density within this work: a) ab-initio simulation, configuration iii, $Co_{43}Fe_{20}Ta_{5.5}B_{31.5}$, b) ab-initio simulation, configuration iii, $Co_{45.5}Fe_{24}Ta_6B_{24.5}$, c) experimental results obtained by nanoindentation and XRR (Cu K$_\alpha$), in comparison to Ref. [103] (dashed line) and Ref. [18] (dotted line).

Results and Discussion

	ab-initio		experimental		
	this work, configuration (iii)		this work	[103]	[18]
	$Co_{43}Fe_{20}Ta_{5.5}B_{31.5}$	$Co_{45.5}Fe_{24}Ta_6B_{24.5}$			
B [GPa]	209	190			
ν	0.283	0.280			
E_r [GPa]			207		
E [GPa]	273	251	233	268	166
ρ [g/cm³]	8.19	8.42	8.80[a]/8.62[b]	8.65	

Table 4-2: *Obtained results for bulk modulus, Poisson's ratio, reduced Young's modulus, Young's modulus and density*
[a] this work by XRR, Cu Kα
[b] this work by XRD, high energy photons

4.2.2 STRUCTURE

For further evaluation of the here proposed *ab-initio* molecular dynamics model, the computationally obtained total PDF and the PDF extracted from X-ray diffraction experiments using high-energy photons were compared. This approach was successfully implemented to characterize the (chemical) short range order of binary metallic glass systems by Sheng et al. [47]. The comparison of the computationally obtained PDF (obtained by analyzing the *ab-initio* model using Equation 3-5)) and the experimental one, is given in Figure 4-3. Both curves exhibit similar characteristic features indicating a valid replication. This provides strong backing of the first principles approach and its feasible implementation for short range order analysis of the quaternary, magnetic amorphous alloy studied here. Nearest neighbor analysis of the *ab-initio* data reveals that the dominant atomic pairs which determine the first coordination shell are (Co,Fe)-(Co,Fe), (Co,Fe)-Ta and Ta-Ta. The small pre-peak located at 2.10 Å can be assigned to the presence of (Co,Fe)-B atomic pairs (see Table 4-3). These results are consistent with experimental PDF analysis employing a hard sphere approach (sum of Goldschmidt radii in combination with X-ray weighting factors) as well as with the results obtained by Kaban et al. [49] utilizing the reverse Monte Carlo method. Relatively large standard deviations on (Co,Fe)-Ta interactions in this study may be due to the limited number of Ta in the supercell, causing poor statistics.
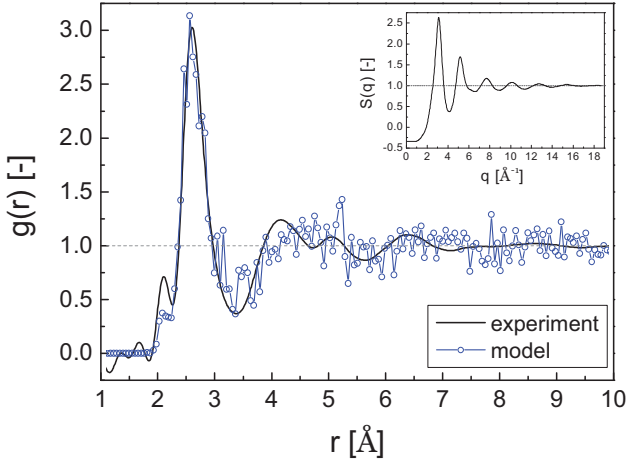
Figure 4-3: *Computationally obtained total PDF (configuration iii, $Co_{45.5}Fe_{24}Ta_6B_{24.5}$) and PDF extracted from X-ray diffraction experiments using high-energy photons. The structure factor $S(q)$ of the amorphous thin film metallic glass is shown in the inset.*

atomic pair	d_{ij} [a] [Å]	standard deviation d_{ij}	R_{ij} [b] [Å]	w_{ij} [b] [-]	r_{ij} [c] [Å]
Fe-B/B-Fe	2.20	0.15	2.07	0.02022	2.20
Co-B/B-Co	2.00	0.09	2.08	0.05404	2.02
Co-Co	2.40	0.10	2.50	0.29418	2.52
Co-Fe/Fe-Co	2.39	0.14	2.49	0.22021	2.51
Fe-Fe	2.45	0.10	2.48	0.04121	2.51
Co-Ta/Ta-Co	2.68	0.24	2.68	0.22216	2.69
Fe-Ta/Ta-Fe	2.71	0.25	2.67	0.08315	2.73

Table 4-3: *Mean nearest neighbor distance d_{ij} for $Co_{45.5}Fe_{24}Ta_6B_{24.5}$ metallic glass*
  [a] this work, ab-initio model
  [b] sum of Goldschmidt's radii R_{ij} (1.25, 1.24, 1.43 and 0.88 Å for Co, Fe, Ta and B respectively) and corresponding X-ray weighting factors w_{ij} calculated at $q=0$ $Å^{-1}$
  [c] mean nearest neighbor distances r_{ij} [49]

The inset of Figure 4-3 shows the structure factor $S(q)$ of the amorphous thin film metallic glass. The sample exhibits a pronounced diffuse scattering pattern typical for metallic glasses with a maximum at $q \sim 3.1$ $Å^{-1}$ and pronounced oscillations visible up to $q \sim 18.5$ $Å^{-1}$. Further Fourier transformation of the structure factor, according to Equation 3-3, leads to the reduced pair distribution function $G(r)$, which, in this case, indicates a missing of long-range order, which again is specific for metallic glasses (data not shown here). As an additional

Results and Discussion

argument for the validity of the *ab-initio* model, a mean atomic density of $\rho_0=0.0944$ atoms/Å^3 (obtained by fitting G(r) on low r-range $\langle 0, 1.8 \rangle$ Å to the equation $-4\pi r \rho_0$) or a respective mass density of 8.62 g/cm^3 was extracted from these XRD experiments, which differs to the thin film density obtained by the X-ray reflectivity technique (Cu K$_\alpha$) by 2%, to the theoretical results by 2-5% depending on the simulation configuration and by only 0.4% to the reported bulk metallic glass density [103].

4.2.3 ELASTICITY

While the bulk modulus is calculated to be 209 GPa by *ab-initio* molecular dynamics for $Co_{43}Fe_{20}Ta_{5.5}B_{31.5}$ and 190 GPa for $Co_{45.5}Fe_{24}Ta_6B_{24.5}$, a reduced Young's modulus of 207±10 GPa was measured experimentally. The Poisson's ratio of $Co_{43}Fe_{20}Ta_{5.5}B_{31.5}$ metallic glass has not been reported in literature. Based on the calculation of Grüneisen constant [148], the Poisson's ratio can be extracted from the energy-volume curves. With the calculated Poisson's ratios of 0.283 and 0.280 for both configurations, nominal and experimental, respectively, one is able to extract the Young's modulus from the reduced Young's modulus value obtained by nanoindentation experiments as well as from computationally obtained bulk modulus using the isotropic approximation.

From the reduced Young's modulus, a Young's modulus of 233±14 GPa is derived using the calculated Poisson's ratio of 0.28. A deviation of 13% with respect to the reported modulus of 268 GPa for $Co_{43}Fe_{20}Ta_{5.5}B_{31.5}$ by Inoue et al. [103] is obtained. The derived Young's moduli of 273 and 251 GPa from the calculated bulk moduli for $Co_{43}Fe_{20}Ta_{5.5}B_{31.5}$ and $Co_{45.5}Fe_{24}Ta_6B_{24.5}$ deviate to the reported bulk value [103] by only 2% and 6%, respectively. The deviation between the *ab-initio* study data for $Co_{43}Fe_{20}Ta_{5.5}B_{31.5}$, $Co_{45.5}Fe_{24}Ta_6B_{24.5}$ and the indentation data for $Co_{45.5}Fe_{24}Ta_6B_{24.5}$ is about 15% and 7%, respectively. Elasticity results are shown in Figure 4-2; see Table 4-2 for all results reported in this study. The magnitude of the largest deviations reported between calculations and experiments is well within the expected range for the exchange correlation functionals used [149]. The differences observed for density and elasticity within both configurations probed in the *ab-initio* study are small, but significant. Similarly to the density data and the short range order data good agreement between the calculated and measured elastic properties could be observed. Altogether it can be summarized, that the here established computational model is useful to describe the elasticity of Co-Fe-Ta-B metallic glass.

In order to correlate the elasticity data presented above with the electronic structure, density of states are studied. Figure 4-4 shows the total density of

states for $Co_{45.5}Fe_{24}Ta_6B_{24}$ as well as total and partial total density of states for the simulated $Co_{43}Fe_{20}Ta_{5.5}B_{31.5}$ metallic glass. Only orbitals with the largest density of states are plotted: 3d for Fe and Co, 5d for Ta as well as 2s and 2p orbitals for B.
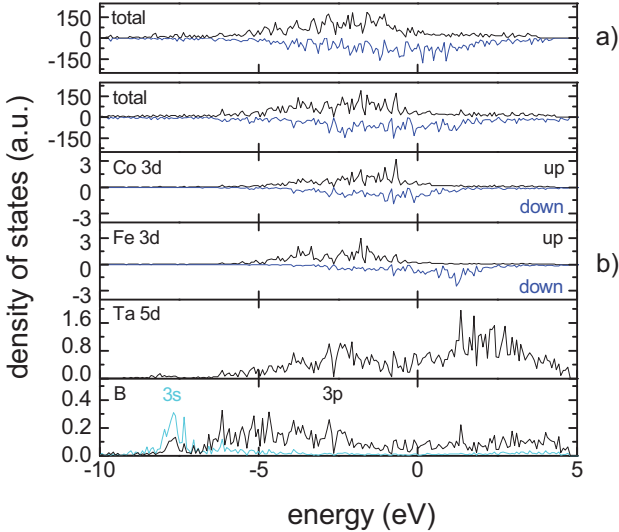
Figure 4-4   a) Total density of states for configuration (iii), $Co_{45.5}Fe_{24}Ta_6B_{24.5}$, b) total and partial density of states for configuration (iii), $Co_{43}Fe_{20}Ta_{5.5}B_{31.5}$. Fermi level is set to 0 eV. Up and down states are provided as positive and negative values, respectively.

It can be seen that the total bonding character is metallic in both Co-Fe-Ta-B compositions since the Fermi level is occupied. This overall (inter-)metallic character gives rise to the large Poisson's ratio, as discussed above. No significant difference in bonding can be identified between the two compositions investigated based on the total density of states. Hence, the properties investigated may be insensitive to compositional variations, as discussed above. The bonds are mainly characterized by the strong interaction between cobalt and iron, as can be seen in the partial density of states of $Co_{43}Fe_{20}Ta_{5.5}B_{31.5}$. Fe-B and Co-B are the strongest hybridized states present; these boron clusters are again metallically bonded. The electronic structure data obtained here are in agreement with the pair distribution analysis conducted in this study and with literature [49], where Co-B bonds are reported to yield the shortest interatomic distance followed by B-B and Fe-B and thus indicate strong bonding. Hence, this fact is expected to be responsible for the large stiffness of this glass.

Results and Discussion

4.3 Experimental Validation: Co-Fe-Ta-Si

In the previous chapter on Co-Fe-Ta-B, (chemical) short range order, density and elastic properties were successfully simulated by *ab-initio* molecular dynamics. The presented model is now utilized to study Co-Fe-Ta-Si glassy alloys. Within this chapter the previously adopted theoretical strategy will be utilized in combination with combinatorial thin film experiments to validate the computational model and to investigate the impact of the metalloid replacement of B with Si on density, elastic and magnetic properties.

The composition of $Co_{49}Fe_{23.5}Ta_6Si_{21.5}$ for the thin film was measured using the atom probe technique. X-ray diffraction measurements, using a gracing incidence angle setup, provide no evidence for the presence of long range order. The final configuration of the molecular dynamics cell does not exhibit any global ordering or decomposition to thermodynamically stable compounds and hence seems to emulate an amorphous compound. Based on the composition and structure data it is evident that metallic glasses with a Si concentration exceeding the bulk samples by ~15 at% can be grown by magnetron sputtering. This can be understood by considering that the cooling rates during vapor phase condensation may reach 10^{15} K/s [125].

4.3.1 Density

From energy-volume-curves, a density of 8.03 g/cm³ is obtained for $Co_{49}Fe_{23.5}Ta_6Si_{21.5}$ by *ab-initio* molecular dynamics. The experimentally obtained X-ray reflectivity value of 8.08 g/cm³ (using a Philips PW1820 diffractometer with Cu K_α radiation and subsequent fitting of the experimental curves by the GenX software [145]) deviates by 0.6% from the calculated density. The theoretical as well as experimental densities show decreasing values as boron is substituted by silicon in Co-Fe-Ta-(B/Si). The relative deviation to the B-containing glass is ~8% based on the XRR results for the $Co_{45.5}Fe_{24}Ta_6B_{24.5}$ and $Co_{49}Fe_{23.5}Ta_6Si_{21.5}$ thin films. The respective computational models of Co-Fe-Ta-(B/Si) deviate by ~5%. This may simply be understood by considering the ionic radii differences between B and Si. See Table 4-4 for the density data obtained in this work in comparison to the already reported values for $Co_{43}Fe_{20}Ta_{5.5}B_{31.5}$ and $Co_{45.5}Fe_{24}Ta_6B_{24.5}$, respectively. Hence, this computational study on Co-Fe-Ta-Si underlines that the theoretical approach to simulate metallic glasses can be used to predict general trends in density when varying the alloy constituents.

		Co-Fe-Ta-Si		Co-Fe-Ta-B			
		ab-initio[1]	exp.[1]	*ab-initio*[2a]	*ab-initio*[2b]	exp.[2b]	exp.[3]
B		164		209	190		
ν		0.31		0.28	0.28		
E_r			167			207	
E		187	177	273	251	233	268
ρ		8.03	8.08	8.19	8.42	8.80	8.65
M	0 K	0.089					
	10 K		0.090				
	300 K		0.075				

Table 4-4: Comparison of theoretical and experimental values of moduli in GPa (B – bulk modulus, E_r – reduced Young's modulus, E – Young's modulus), Poisson's ratio (v), densities in g/cm^3 (ρ) and volume magnetization (M) in $\mu_B/Å^3$. 1: $Co_{49}Fe_{23.5}Ta_6Si_{21.5}$, 2(a): $Co_{43}Fe_{20}Ta_{5.5}B_{31.5}$ and (b) $Co_{44.5}Fe_{24}Ta_6B_{24.5}$ [104]. 3: bulk experiment on $Co_{43}Fe_{20}Ta_{5.5}B_{31.5}$.

4.3.2 ELASTICITY

A bulk modulus value of 164 GPa is obtained from energy-volume curve analysis using the Birch-Murnaghan equation of states [129] for the simulated $Co_{49}Fe_{23.5}Ta_6Si_{21.5}$ metallic glass. A reduced Young's modulus of 167±10 GPa is obtained by depth-sensing nanoindentation (Hysitron TriboIndenter™, Berkovich indenter tip) for the as grown thin film. Details on the experimental procedure can be found in chapter 3.2 [104].

The Poisson's ratio of Co-Fe-Ta-Si metallic glass has been extracted from energy-volume curves and determined based on the calculation of Grüneisen constant [148]. With this Poisson's ratio of 0.31 one is able to extract the Young's modulus from reduced Young's modulus obtained by nanoindentation experiments ($E(E_r)$) as well as from computationally obtained bulk modulus using the isotropic approximation (E(B)). Hence, a derived E(B) of 187 GPa is obtained. The deduced Young's modulus of 177±12 GPa from the experimentally measured reduced Young's modulus deviates to the theoretical value by 5%. The agreement between E(B) and $E(E_r)$ for $Co_{49}Fe_{23.5}Ta_6Si_{21.5}$ underlines that the methodologies used here are reasonable and go well together with the already reported results for the Co-Fe-Ta-B metallic glass [104]. The boron-containing metallic glass is by 19% stiffer than Co-Fe-Ta-Si (the nanoindentation data are compared). Based on this approach to replace boron by silicon in the Co-Fe-Ta-B system, a correlation between density and stiffness can be established. Correlations between density and elastic properties have been reported for crystalline and amorphous alumina [150] and silica [151], amorphous SiC [152] and amorphous boron suboxides [153, 154] as well. These foresaid systems exhibit a direct dependency of bulk

Results and Discussion

and Young's modulus on density. The same correlation for the B and Si containing metallic glasses under study may point to the fact that density might play an important role when designing metallic glasses.
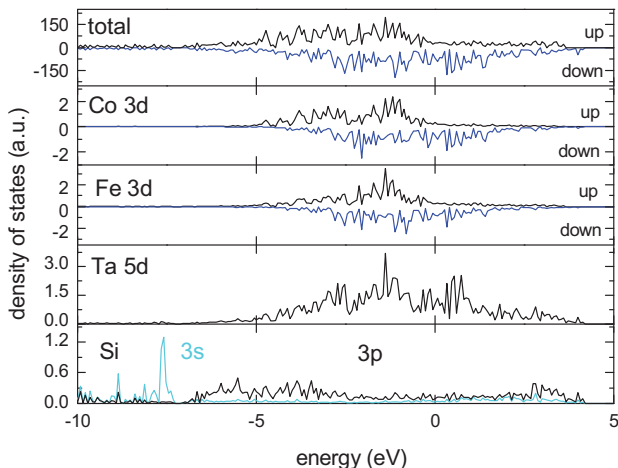
Figure 4-5: Total and partial density of states for $Co_{49}Fe_{23.5}Ta_6Si_{21.5}$ obtained by ab-initio molecular dynamics. Fermi level is set to 0 eV, up and down states are provided as positive and negative values, respectively.

Figure 4-5 shows the total as well as partial density of states for the theoretically investigated $Co_{49}Fe_{23.5}Ta_6Si_{21.5}$ system. Analysis of these data allows for a correlation of the electronic structure with elastic properties. Orbitals showing the highest density of states were plotted: 3d for Co and Fe, 5d for Ta and 3s and 3p for Si. The total character is metallic, since the Fermi level is occupied. Strong interactions between Fe and Si, as well as between Co and Si yield the major contribution to this (inter-)metallic like bond character; they are the strongest hybridized states and form silicon clusters which are again metallically bonded. The strong bonding present, also reflected in a comparatively large Poisson's ratio, results in the large bulk modulus. An (inter-) metallic character has also been reported for Co-Fe-Ta-B [104], mainly caused by Co-B bonds in this case. The strongest hybridized states in the boron-containing glass were identified to be Co-B and Fe-B, respectively. Comparing the results of both metallic glass systems (Co-Fe-Ta-Si and Co-Fe-Ta-B) agreement with literature is observed: Qin and co-authors suggest a Fe-Si/Fe-B cluster formation based on the density of states [66]. Moreover, they report Fe-Si bonds to be stronger than Fe-B bonds [66]. Both observations are supported by this study. A direct comparison of the

bonding strength of X-Si to X-B (X=Co,Ta), as obtained in the studies presented here, shows that X-Si bonds are weaker. Due to the composition of the metallic glasses under study, these atomic pairs may outnumber the stronger Fe-Si bonds, which may give an explanation for the decrese in stiffness.

4.3.3 MAGNETIZATION

To obtain the volume magnetization of the deposited thin film, SQUID measurements were carried out, using a Quantum Design MPMS system at 10 and 300 K. The volume magnetization data are listed in Table 4-4 and shown in Figure 4-6.
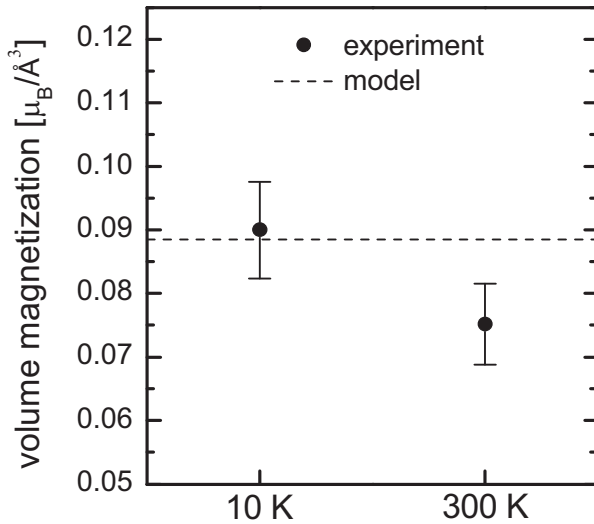
Figure 4-6: Results from thin film magnetization measurements compared to the simulation for $Co_{49}Fe_{23.5}Ta_6Si_{21.5}$.

If the experimental values obtained at 10 K are compared to the theoretical value from the first principles model (0 K), a deviation of 1.1% is obtained. By decreasing the temperature during the measurements from 300 to 10 K towards the theoretically used 0 K, the deviation is reduced. Hence, good agreement is observed.

4.4 IMPLEMENTATION OF THE MODEL: CO-FE-TA-X (X=B,SI,P,S)

After the successful validation of the computational model by experimental replication of Co-Fe-Ta-(B/Si) thin film PDFs, densities, elasticity and

Results and Discussion

magnetization data, bonding nature and internal atomic arrangements, elastic as well as magnetic properties are analyzed within this chapter in terms of density of states, effective charge, pair distribution functions as well as bulk modulus and transition metal magnetic moments. All characteristics are studied as a function of X and hence of valence electron concentration and atomic size within $Co_{43}Fe_{20}Ta_{5.5}X_{31.5}$ (X=B,Si,P,S).

4.4.1 BONDING ANALYSIS

The electronic structure will be analyzed first. In Figure 4-7 partial DOS are plotted for all alloys studied. Only the orbitals exhibiting the highest population are taken into account: 3d for Co and Fe, 5d for Ta and 3s/3p for B/Si/P/S. The metallic character is present in all four systems probed: the occupied states around the Fermi level are consistent with a metallic bonding. In chapter 4.2.2 [104], strong interactions between Co and B as well as Fe and B were described. Here, in analogy, strong interactions between Co and X as well as Fe and X (X=Si,P,S) can be identified contributing towards the overall (inter-) metallic character of $Co_{43}Fe_{20}Ta_{5.5}Si_{31.5}$, $Co_{43}Fe_{20}Ta_{5.5}P_{31.5}$ and $Co_{43}Fe_{20}Ta_{5.5}S_{31.5}$. Co and X as well as Fe and X atoms form clusters interconnected via metallic bonds. Co-B as well as Fe-B are already reported to be the strongest hybridized states [104] in the previous discussion in chapter 4.2.2, which is now shown to be valid for X=Si, P and S, too. The strongest hybridization within (Co,Fe)-X (X=B,Si,P,S) is identified to be Co-S, followed by Co-B, Fe-P and Fe-Si. The states of cobalt and iron are spin polarized for all configurations probed. A replacement of B by Si in particular, introduces a strong magnetic polarization, observable as intense peaks in the up and down states (see Figure 4-7).
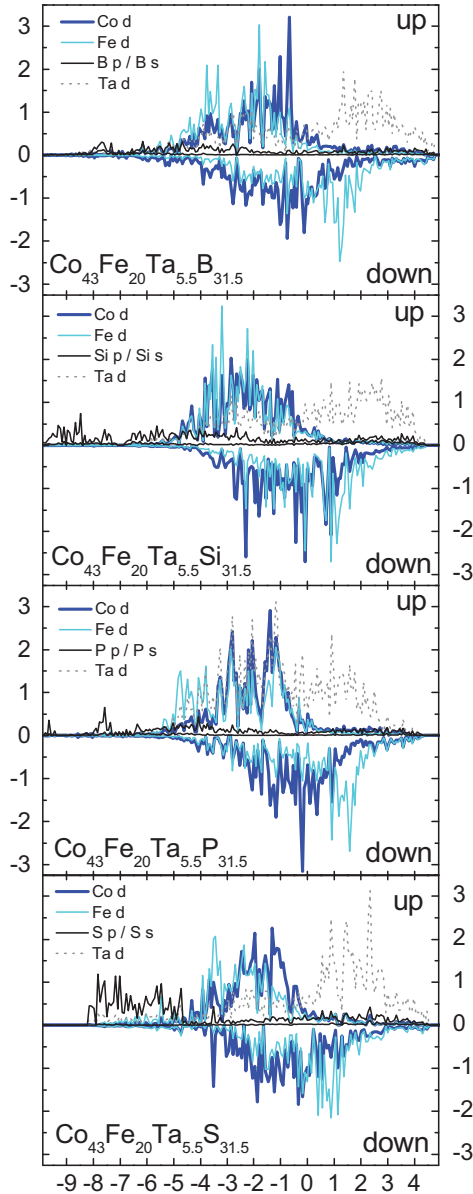
Figure 4-7: Partial density of states for $Co_{43}Fe_{20}Ta_{5.5}X_{31.5}$ (X=B,Si,P,S) investigated in this study. Co d states are displayed as bold solid, Fe d as bright solid, X p and X s states as dark solid and Ta d states as dotted lines. The Fermi level is set to 0 eV. Up and down states of Co and Fe are provided as positive and negative values, respectively.

Results and Discussion

To evaluate ionic contributions, which may be significant for explaining elastic properties the Bader charge analysis is employed to study the changes in the effective charge induced by valence electron concentration variation. Figure 4-8 shows the effective charge as a function of ionic potential of each atomic species for all four configurations probed. The ionic potential is defined as $\Phi=Z/r_{ion}$ (where Z is the effective charge of the ion and r_{ion} is the ionic radius). This ratio is a measure of charge density and ionic interaction.
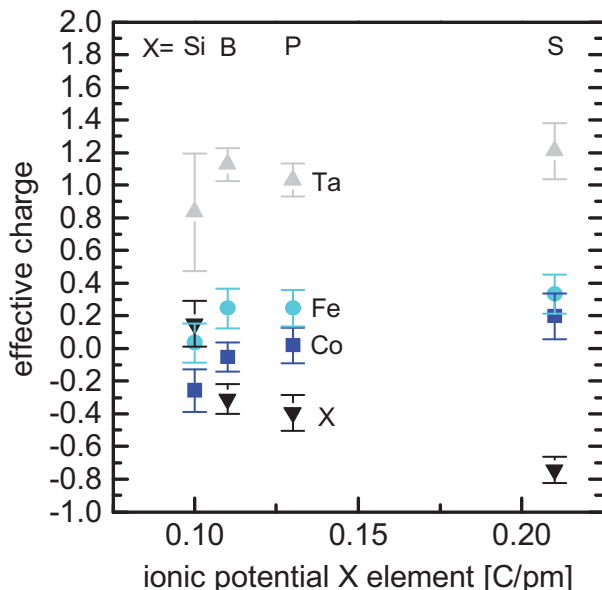
Figure 4-8: *Effective charge of Co (squares), Fe (circles), Ta (upward facing triangles), B, Si, P and S (downward facing triangles) as a function of ionic potential of the X element for all probed configurations $Co_{43}Fe_{20}Ta_{5.5}X_{31.5}$ (X=B,Si,P,S).*

A variation in the ionic potential of X in the range of 0.1 to 0.21 C/pm does not affect the most populated species, Co and Fe to a larger extent. These elements are mainly metallic in nature while the third metal, Ta, is most depleted irrespective of X. The effective charge of the X element, being the second most abundant constituent, is negative in the case of X=B, P and S. It can be seen that an increase in ionic potential when X is systematically varied from Si to B, P and further to S, shifts the general metallic bond character of the simulated metallic glasses towards a more ionic bonding. If B is substituted by Si, resulting in a decrease of the ionic potential for X, fewest effective charges for all constituents can be stated. A further X substitution from Si to P increases the ionic potential of

X from 0.1 to 0.13 C/pm and drastic charge transfer from mainly tantalum to the X element is realized. $Co_{43}Fe_{20}Ta_{5.5}P_{31.5}$ and $Co_{43}Fe_{20}Ta_{5.5}B_{31.5}$ bear resemblance in effective charges of all four constituents. The maximum difference is found to be 0.096 C/pm for Ta in both configurations. A high charge transfer can be further adduced for the X substitution resulting in the $Co_{43}Fe_{20}Ta_{5.5}S_{31.5}$ configuration. The effective charge of S varies with respect to B by 0.43 C/pm. Sulfur as the element exhibiting the highest ionic potential and known for a high electronegativity is expected to form the most ionic bonds for all X elements probed. Hence it can be concluded that a large ionic potential of X results in a strong ionic interaction, which in turn is expected to decrease the stiffness of the amorphous alloys studied.

4.4.2 STRUCTURE AND DENSITY

Pair distribution functions reveal short range order and were successfully employed for the validation of the *ab-initio* model used here [104] as shown in chapter 4.2.2 PDFs are used to gain insight into the X induced changes in short range order by identification of atomic pair interactions.
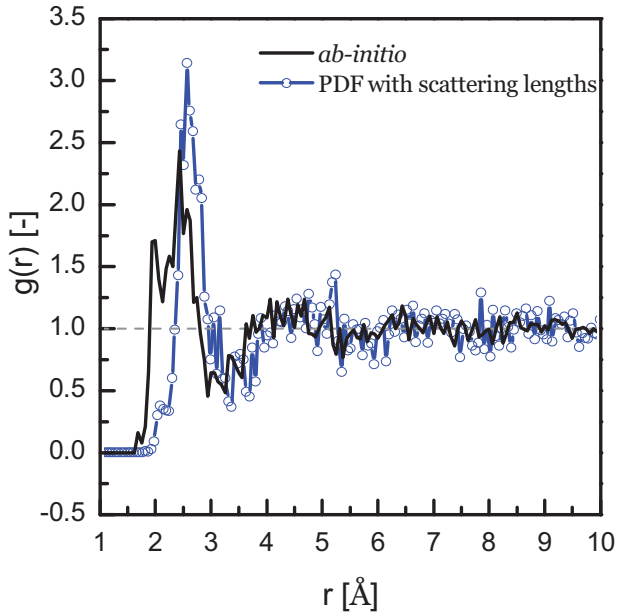
Figure 4-9: Pair distribution function of $Co_{45.5}Fe_{24}Ta_6B_{24.5}$, ab-initio data from VASP (solid) and calculated with scattering lengths (line+circles)

Results and Discussion

Figure 4-9 shows the comparison of two PDFs. The first PDF (solid line) is obtained from *ab-initio* calculations with the VASP code by Fourier transformation of the calculated structure factor, without considering scattering lengths of the corresponding elements [121]. The second PDF shown in Figure 4-9 (line+circles) is obtained based on a calculation in real space, taking type and position of each atom within the supercell into account a. Scattering lengths of the corresponding atomic types are included in this calculation. As one can see, the curve is shifted and the first pre-peak, visible in the *ab-initio* data, vanishes when scattering lengths are included into the PDF calculation. This can be understood by considering the low scattering power of B, which is not considered in the VASP code as all scattering lengths are equal to one [121]. Good agreement is obtained for the X-ray diffraction data with the calculated PDF including the scattering lengths [104]. The fact, that the inclusion of scattering lengths has such a prominent effect on the PDF, is due to the different mass and size and hence scattering power values of the atoms forming this alloy. Nevertheless, we will use *ab-initio* data directly obtained from the VASP code for the structural analysis and discussion on an atomic level of all four systems investigated, as provided in Figure 4-10 to enable the comparison with other computational studies. It is apparent that all configurations studied exhibit no long range order.
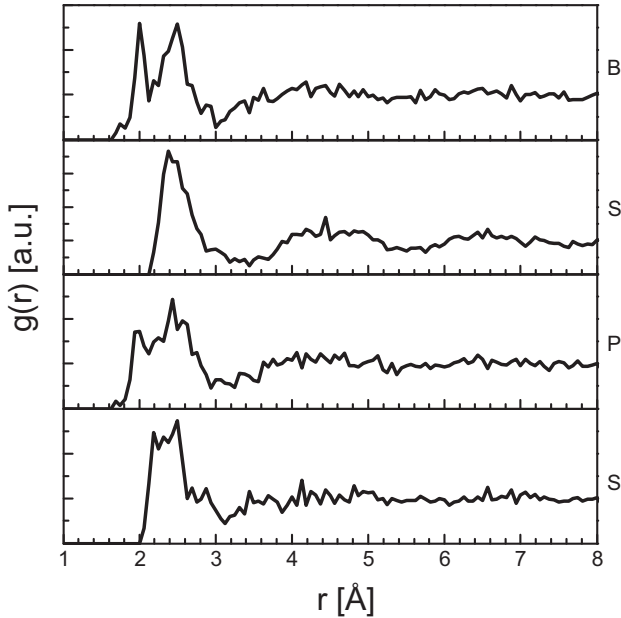
Figure 4-10: Pair distribution functions of $Co_{43}Fe_{20}Ta_{5.5}X_{31.5}$, X=B, Si, P and S

The first coordination shell of $Co_{43}Fe_{20}Ta_{5.5}B_{31.5}$ is of bimodal shape, centered at ~ 2 and 2.5 Å, and is dominantly composed of (Co,Fe)-B and (Co,Fe)-(Co,Fe), (Co,Fe)-Ta and Ta-Ta interactions [104]. The small pre-peak located at 1.73 Å may be assigned to B-B atomic pair correlations [104]. A more detailed analysis on the PDF of the related $Co_{45.5}Fe_{24}Ta_6B_{24.5}$ glassy alloy can be found in chapter 4.2.2 [104].

For the Si containing metallic glass $Co_{43}Fe_{20}Ta_{5.5}Si_{31.5}$, the distribution is unimodal and centered around 2.6 Å, but it can still be subdivided into several contributions. The atomic pairs responsible for the shape of this peak are (Co,Fe,Ta)-Si, Fe-Co and Si-Si. A detailed peak analysis can be found in Table 4-5. As the valence electron concentration is increased by substituting Si with P, the pair distribution function for $Co_{43}Fe_{20}Ta_{5.5}P_{31.5}$ shows a small pre-peak below 2 Å and a pronounced second peak of bimodal shape. As listed in Table 4-5, P-P pairs contribute to the pre-peak, which is in agreement with Ref. [155], while the first feature of the second peak is composed of P-P and Co-P interactions. Hence the P-containing quaternary metallic glass is revealing similarities for the dominating atomic pairs at a certain distance to $Co_{43}Fe_{20}Ta_{5.5}B_{31.5}$. As the valence electron concentration is increased by substituting P with S, the PDF for $Co_{43}Fe_{20}Ta_{5.5}S_{31.5}$

Results and Discussion

shows a rather broad first peak around 2.5 Å. The first three vertices can be attributed to Co-S, Fe-S and a mixture of Ta-S, Fe-Fe-, Co-Co and Co-Fe interactions as listed in Table 4-5. The shoulder to the right arises from Co-Ta and Co-Co atomic pairs. It is noteworthy to mention, that for $Co_{43}Fe_{20}Ta_{5.5}S_{31.5}$ no S-S interaction could be identified. While $Co_{43}Fe_{20}Ta_{5.5}B_{31.5}$ and $Co_{43}Fe_{20}Ta_{5.5}P_{31.5}$ show similarities the shape of PDFs and hence in nearest neighbors which account for short range order, the same can be stated for $Co_{43}Fe_{20}Ta_{5.5}Si_{31.5}$ and $Co_{43}Fe_{20}Ta_{5.5}S_{31.5}$. Atomic pairs which possess strong bonds according to DOS analysis reveal indications for interactions in the PDFs as well. Namely, (Co,Fe)-X (X=B,Si,P,S) are identified to form strong and short bonds based on both DOS and PDF data.

Pairs i,j	$Co_{43}Fe_{20}Ta_{5.5}B_{31.5}$				$Co_{43}Fe_{20}Ta_{5.5}Si_{31.5}$			$Co_{43}Fe_{20}Ta_{5.5}P_{31.5}$			$Co_{43}Fe_{20}Ta_{5.5}S_{31.5}$		
	d_{ij} [Å]	σ(d) [Å]	N_{ij}/N_{ji}	Ref. [49]	d_{ij} [Å]	σ(d) [Å]	N_{ij}/N_{ji}	d_{ij} [Å]	σ(d) [Å]	N_{ij}/N_{ji}	d_{ij} [Å]	σ(d) [Å]	N_{ij}/N_{ji}
X-X	1.84	0.08	1.1	2.3	2.60	0.17	2.9	2.08	0.31	1.6	-	-	-
Fe-X/X-Fe	2.17	0.11	2.9/1.9	2.3/1.5	2.45	0.10	3.6/2.4	2.25	0.20	2.6/1.7	2.27	0.13	2.6/1.7
Co-X/X-Co	2.01	0.05	3.1/4.4	3.7/5.1	2.33	0.08	4.0/5.8	2.05	0.18	3.4/4.8	2.23	0.10	3.2/4.6
Ta-X/X-Ta	2.53	0.14	4.1/0.8	2.9/0.5	2.78	0.22	4.6/0.9	2.29	0.20	4.0/0.8	2.59	0.15	4.1/0.8
Fe-Fe	2.50	0.10	2.8	4.6	2.51	0.22	2.8	2.46	0.14	3.0	2.51	0.21	1.9
Fe-Co/Co-Fe	2.39	0.12	6.0/2.8	5.6/2.6	2.41	0.17	5.0/2.3	2.41	0.14	6.1/2.8	2.48	0.23	4.8/2.3
Fe-Ta/Ta-Fe	2.71	0.16	0.9/2.7	1.1/4.0	2.63	0.17	0.8/2.6	2.55	0.17	0.8/2.6	2.77	0.24	0.8/2.4
Co-Co	2.41	0.07	5.5	7.0	2.46	0.11	4.6	2.41	0.10	5.1	2.47	0.14	4.2
Co-Ta/Ta-Co	2.63	0.23	1.1/7.4	1.0/8.1	2.66	0.24	0.9/6.1	2.52	0.23	0.8/5.6	2.69	0.25	0.7/4.7

Table 4-5: Mean nearest neighbor distances $d_{i,j}$, their standard deviations σ (d) and coordination numbers N_{ij}/N_{ji} for $Co_{43}Fe_{20}Ta_{5.5}X_{31.5}$ metallic glasses calculated in this study and Ref. [49].
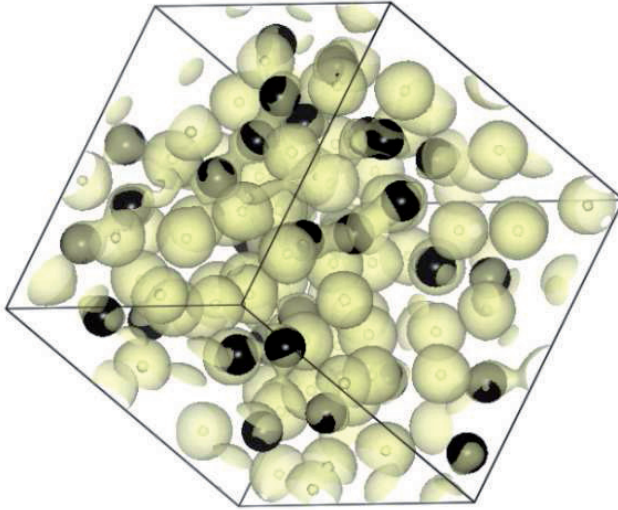
Figure 4-11: Isosurfaces of electron density for $Co_{43}Fe_{20}Ta_{5.5}B_{31.5}$ (equi-density level of 0.095 [a.u.]). Solely B atoms are displayed for clarity using the VESTA software [156].

The extracted coordination numbers (N_{ij}) for the $Co_{43}Fe_{20}Ta_{5.5}B_{31.5}$ metallic glass simulated in this study agree well with the values reported by Kaban et al. [49] (see Table 4-5) Maximum deviations are observed for Ta containing correlations, which may be due to the limited amount of Ta atoms present in the supercell, causing poor statistics. B-B pairs are found to be present in the model, which is consistent with the data reported by Kaban et al. [49]. N_{BB} is extracted to be 1.1, which is in agreement with Pusztai and Sváb [157], where $N_{BB} \approx 1$ was obtained from reverse Monte Carlo simulations of $Ni_{65}B_{35}$. Short boron chains have formed in the B containing system (see Figure 4-11): Here B atoms are displayed as black spheres, surrounded by their electron density isosurfaces, indicated as halos. Interconnected isosurfaces suggest chemical bonding between the respective atoms. The here observed formation of B chains is in agreement with Ref. [157] and Ref. [158], while no evidence for the formation of a B network as suggested by Kaban et. al for $N_{BB}=2.3$ [49] could be identified.

As the valence electron concentration is increased by substituting B with Si, an increase in coordination number can be observed for (Co,Fe,Ta,X)-X and X-(Co,Fe) (X=B,Si) pairs as listed in Table 4-5. The aspect of an increased coordination number for X=Si is further supported by a total coordination number analysis for X in all four configurations under study: $<N_X>=8.2/12.0/8.9/7.1$ for X=B/Si/P/S, respectively and it is hence obviously higher for the Si containing glass. The total

Results and Discussion

coordination number of 12.0 for Si is large compared to $<N_B>$, $<N_P>$ and $<N_S>$ and furthermore in the same range as $<N_{Co}>$ and $<N_{Fe}>$. The already discussed similarity for the B and P containing metallic glasses as well as for $Co_{43}Fe_{20}Ta_{5.5}X_{31.5}$ (X=Si,S) in terms of short range ordering is also observed within the coordination number data obtained from the PDF data (see Table 4-5).

After discussing the chemical bonding of the quaternary amorphous alloys, densities as given in Table 4-6 will be analyzed next.

	Co-Fe-Ta-B[1]	Co-Fe-Ta-Si	Co-Fe-Ta-P	Co-Fe-Ta-S
cohesive energy/atom [eV]	-7.4552	-7.1529	-7.4592	-6.6234
B [GPa]	209[1]	168	161	118
ρ [g/cm³]	8.19[1]	8.07	7.62	7.15
cell volume [Å³]	1157	1395	1435	1537
	B	Si	P	S
valence electrons	3	4	5	6
ionic radius [pm]	27[2]	40[2]	38[2]	29[2]
ionic potential [C/pm]	0.11	0.10	0.13	0.21

Table 4-6: Theoretical results of the quaternary systems investigated in this study , as well as number of valence electrons and 2: ionic radii (Ref [159]), for X=B, Si, P and S.

The densities extracted from the theoretical models decrease steadily when B is substituted by Si, P and S. For $Co_{43}Fe_{20}Ta_{5.5}B_{31.5}$ a density of 8.19 g/cm³ can be reported, the S containing glass gives a density of 7.15 g/cm³, which implies a reduction of 12.7%. The covalent radii of Si, P and S increase by 35%, 29% and 24% as compared to the B radius. Although there is a decreasing trend in radius gain when the X element is substituted by Si, P and further by S, the density of each metallic glass is decreasing. This may be understood by an increase in average bond length and/or the formation of cavities. An increase of bond length may be causative for the density decrease in $Co_{43}Fe_{20}Ta_{5.5}P_{31.5}$ and $Co_{43}Fe_{20}Ta_{5.5}S_{31.5}$ compared to $Co_{43}Fe_{20}Ta_{5.5}B_{31.5}$. The analysis shows that the averaged and weighted distances increase by 2.4% and 5.5%, respectively (all pairs with Ta atoms were neglected, due to the limited amount of atoms, as already discussed above). A corresponding decrease of 7% and 13% in density correlates well with the changes in distances since they result in a density decrease of 7% and 17%. For $Co_{43}Fe_{20}Ta_{5.5}Si_{31.5}$ it may be speculated that cavities cause a slight decrease in density of 1.5% (compared to the B containing glass), although the net atomic distances increase by 11%. The increase in atomic radius of Si by 35% as compared to B and higher coordination numbers for (Co,Fe,Ta)-Si and Si-(Co,Fe) pairs may support this speculation. A correlation of

coordination and the presence of cavities is reported in Ref. [47] as well, where cavities are linked with the packing of quasi-equivalent clusters. By also taking the results of coordination analysis into account, one may thus postulate a non-uniform packaging of clusters and cavities for the Si containing amorphous alloy.

4.4.3 ELASTICITY

The bulk moduli, provided in Table 4-6, decrease when X is varied within $Co_{43}Fe_{20}Ta_{5.5}X_{31.5}$ from B to Si, P and S and are in the range of 118-209 GPa. To analyze this trend, the bulk moduli are correlated with density and cohesive energy, as shown in Figure 4-12.
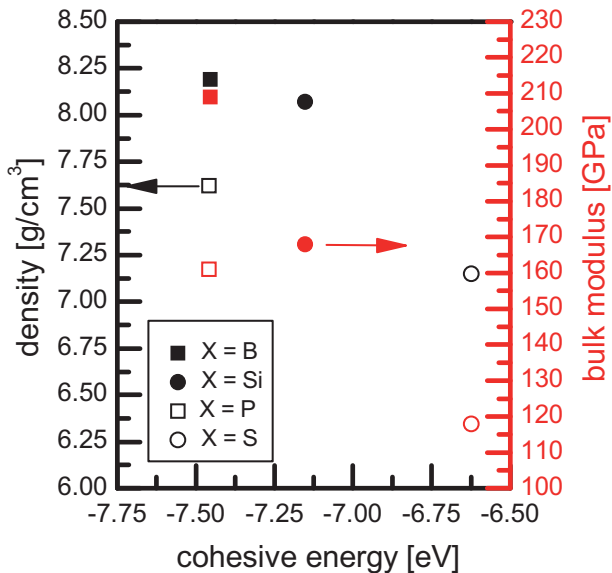
Figure 4-12: Density as well as bulk modulus plotted versus cohesive energy for all systems probed in this study.

As the valence electron concentration increases when X is varied from B to Si and S, a decreasing trend in cohesive energy is accompanied by an increase in bulk modulus. This is consistent with other amorphous systems, such as B_6O [153], Al-O-H [150] and crystalline systems, for example Al_2O_3 [160]. The decreasing stiffness as a function of VEC is also consistent with the VEC induced increase in ionic bond character (see Figure 4-8). The deviant behavior for X=P may stem from the size differences. For instance, it is known that the cohesive energy of

Results and Discussion

small diamond and large Nb are -7.37 and -7.57 eV, while their bulk moduli are 443 and 170 GPa [161]. More work is needed to analyze the anomaly for X=P.

4.4.4 MAGNETIC PROPERTIES

Figure 4-13 shows the normalized magnetic moments of Fe and Co within all four metallic glasses under study with respect to the magnetic moments of pure (bcc) Fe and (hcp) Co, respectively.
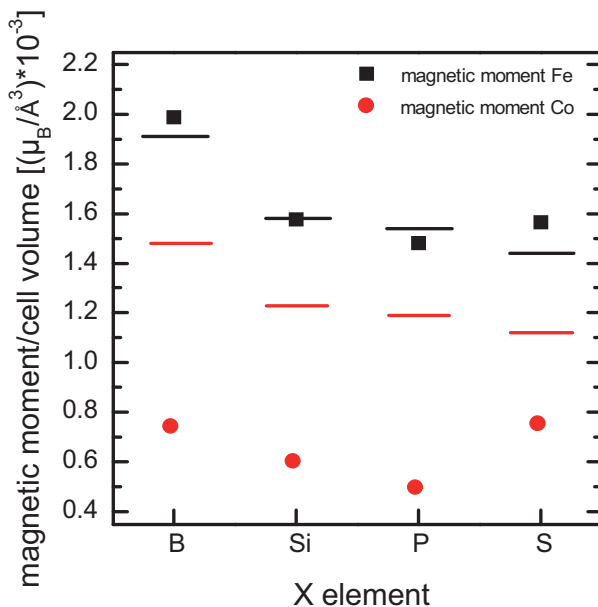
Figure 4-13: Normalized magnetic moment of Fe and Co for all four systems probed with reference to the normalized magnetic moment of pure elements (horizontal lines).

The magnetic moment of Fe in these quaternary glasses is not significantly affected with respect to the value of pure Fe. The highest magnetic moment of Fe can be reported for the sulfur containing alloy, while the other modifications give a ~ 4.4-11.6% lower value. A more drastic change is observed for Co. The magnetic moment appears to be significantly lower than the reference value of pure Co. The largest variation in normalized Co magnetic moment with reference to the pure element is observed for $Co_{43}Fe_{20}Ta_{5.5}B_{31.5}$. Within the alloys studied here maximum deviation in magnetic moments of 34% is identified for $Co_{43}Fe_{20}Ta_{5.5}S_{31.5}$ and $Co_{43}Fe_{20}Ta_{5.5}P_{31.5}$, while $Co_{43}Fe_{20}Ta_{5.5}S_{31.5}$ is still 33% lower

than the reference magnetic moment for pure cobalt. The observation that the magnetic moment of Co is reduced may be explained by the fact that metalloid elements seem to reduce the magnetic moments of the transition metals within amorphous metallic alloys [162]. Ferromagnetism occurs due to unpaired d electrons, so the discussion of the magnetic moment values will be based on the electronic structure. The DOS extracted from the *ab-initio* simulations agree well with the approach of Alben [163] that sp metalloid electrons hybridize with s/p/d electrons of the transition metals and form covalent bonds below the Fermi level as well as antibonding interactions above. When electrons move from these antibonding sites to the d-bands of Co, the magnetic moment will be reduced due to lowering of unpaired states, despite the fact that hardly any charge transfer is realized. Detailed analysis of the effective charge transfer, as well as an integration of the d-bands of Co, support this notion, indicating no drastic variation in charge for Co and less filled Co states for $Co_{43}Fe_{20}Ta_{5.5}S_{31.5}$ and hence the lowest reduction of the magnetic moment for Co within $Co_{43}Fe_{20}Ta_{5.5}X_{31.5}$ (X=B,Si,P,S) metallic glasses. Furthermore, this fact corroborates the reduction of bulk modulus when X is varied from B to Si, P and S: the interaction between X and the transition metal becomes less strong due to less electron transfer from X to the d bands of Co and Fe and hence a weaker s-d hybridization [101, 164]. The interplay between transition metal d band filling and s-d hybridization seems to be a key design criterion for high strength and soft magnetic metallic glasses.

4.4.5 EXTENDED DIAGONAL RELATIONSHIP BETWEEN B AND P

The similarities in effective charges of all four constituents, PDF shape, nearest neighbors and coordination number data between $Co_{43}Fe_{20}Ta_{5.5}B_{31.5}$ and $Co_{43}Fe_{20}Ta_{5.5}P_{31.5}$ as discussed above may be caused by the similar ionic potential (ratio between ionic radius and ionic charge). This phenomenon, known as the so called "diagonal relationship" [165-168] mainly occurring between elements of the second and third period, states that diagonally neighboring elements show similar chemical behavior. For instance, Be is more similar to Al than to B. Here, the addition of one valence electron is compensated by the larger ionic radius of Al. Hence, the ionic potentials of Be and Al are similar, resulting in similar properties [165, 166]. Although B and P are not directly adjacent, the ionic potentials for B and P are as close as for B and Si (see Table 4-6). This fact, in combination with the high impact of atomic radii and effective charge on the here investigated properties, may explain the similarity between both metallic glasses $Co_{43}Fe_{20}Ta_{5.5}B_{31.5}$ and $Co_{43}Fe_{20}Ta_{5.5}P_{31.5}$. This is here referred to as an "extended diagonal relationship".

5 CONCLUSIONS

This work presents the generation, validation and implementation of a first principle model for the quaternary $Co_{43}Fe_{20}Ta_{5.5}X_{31.5}$ metallic glasses with X=B, Si, P, S. The *ab-initio* model allows for the identification of valence-electron-concentration and size-induced changes in short range order, charge transfer and bonding nature. A correlation with density, elasticity and magnetism could be established.

Theoretical results for Co-Fe-Ta-X (X=B,Si) were successfully coupled with thin film experiments. X-ray amorphous $Co_{45.5}Fe_{24}Ta_6B_{24.5}$ and $Co_{49}Fe_{23.5}Ta_6Si_{21.5}$ thin film metallic glasses were deposited using combinatorial physical vapor deposition. These films were then employed to validate the computational model with experimental PDF as well as density, elasticity and magnetization data:

Comparison of the experimental PDF with the one obtained by analyzing the *ab-initio* model for $Co_{45.5}Fe_{24}Ta_6B_{24.5}$ shows good agreement and indicates a successful replication of short range order. The density of 8.42 g/cm³ obtained via *ab-initio* molecular dynamics is within 2-4% of the experimentally measured values of 8.62 and 8.80 g/cm³. Good agreement is also observed for the Young's modulus of ~233 GPa obtained via nanoindentation of thin films and the 251 GPa calculated by *ab-initio* molecular dynamics. The deviation between the computationally obtained value for $Co_{45.5}Fe_{24}Ta_6B_{24.5}$ and the experimentally determined stiffness is 7%. Both, density and stiffness values are consistent with previously reported bulk data [103] and can be understood based on the electronic structure. $Co_{45.5}Fe_{24}Ta_6B_{24.5}$ consists of hybridized boron forming Co-B and Fe-B clusters which are metallically interconnected. This overall (inter-)metallic character gives rise to large Poisson's ratio and, due to strong bonding, large stiffness. Hence the properties measured can be understood based on the presence of itinerant (metallic) and localized (hybridized) bonding between the constituents.

The simulation results for $Co_{49}Fe_{23.5}Ta_6Si_{21.5}$ are in agreement with experimental data obtained for the sputtered thin films. The density of 8.03 g/cm³ obtained by simulations is confirmed by an experimentally determined thin film density of 8.08 g/cm³. Good agreement is obtained for elasticity data as well; from the simulations, the bulk modulus was determined to be 164 GPa which is close to the experimentally measured reduced Young's modulus of 167 GPa. Using a calculated Poisson's ratio of 0.31 we obtain 187 and 177 GPa for calculated and measured Young's moduli, respectively. Comparing the results obtained for Co-Fe-Ta-Si to Co-Fe-Ta-B, a decrease in density as well as in Young's modulus, as

Conclusions

determined both by theory and experiments can be reported. The theoretically determined decrease in density and bulk modulus is 4.6% and 25.5%, respectively, while the experimentally obtained relative differences are 8.2% and 24%, respectively, when B is replaced by Si in Co-Fe-Ta-(B/Si). The analysis of the electronic structure may therefore aid the understanding the correlation between the elasticity data and bonding. The Co-Fe-Ta-Si metallic glass offers, as well as the Co-Fe-Ta-B alloy, an overall (inter-)metallic like character and appearance of interconnected clusters, consisting of Co-Si and Fe-Si. Large Poisson's ratio may be explained by this type of bonding, while strong Fe-Si and Co-Si bonds may be responsible for the large stiffness. The fact that silicon is not as strongly bonded to the residual atomic species as boron, may explain the slightly lower stiffness. The volume magnetization of 0.090 $\mu_B/\text{Å}^3$ obtained by SQUID measurements at 10 K and the *ab-initio* value of 0.089 $\mu_B/\text{Å}^3$ are in very good agreement.

The implementation of the successfully validated first principles model reveals that the bulk moduli of all amorphous alloys show a decreasing trend when X is varied from B to Si, P and further to S. This can be understood by analyzing density and cohesive energy: A decrease in bulk modulus is attended by a decrease in density and caused by a weaker cohesion (less negative cohesive energy). Cohesion seems to be influenced by several factors like the hybridization strength of the main constituents, the ionic potentials and the spatial distribution of atoms: A higher hybridization strength between Co and X seems to give rise to a stronger cohesion. Furthermore, a large ionic potential as well as a non-uniform distribution of clusters and cavities seem to reduce cohesion. Density of states as well as PDFs indicate these (Co,Fe)-X atomic pairs to be the shortest and strongest constituents. A Bader charge analysis reveals the trend towards a more ionic bond character as B is substituted by P and S. Density, bond length and coordination number analysis of the amorphous alloy $Co_{43}Fe_{20}Ta_{5.5}Si_{31.5}$ suggests a non-uniform distribution of clusters and cavities, exhibiting a different structural appearance than for the other systems studied. For $Co_{43}Fe_{20}Ta_{5.5}X_{31.5}$ (X=P,S) the increase in atomic distances is accompanied by a proportional decrease in density with respect to $Co_{43}Fe_{20}Ta_{5.5}B_{31.5}$. The reduction of transition metal magnetic moments, especially for Co, may be attributed to the presence of the X element, giving rise to filled d states of Co and hence a diminishment of magnetic moments. This effect is the least pronounced for X=S. Similarities between the two configurations $Co_{43}Fe_{20}Ta_{5.5}B_{31.5}$ and $Co_{43}Fe_{20}Ta_{5.5}P_{31.5}$ may be due to an extended diagonal relationship between B and P caused by similar ionic potentials.

This thesis shows that quantum mechanics enables the identification of composition induced changes in short range order, charge transfer and on bonding nature and the subsequent linking to density, elasticity and magnetism. The interplay between transition metal d band filling and s-d hybridization was identified to be a key materials design criterion. The here revealed property-electronic structure correlations may provide the basis for future knowledge based design of glassy materials.

5.1 OUTLOOK

The here presented *ab-initio* model is validated by experiments and the atomic arrangements within the corresponding supercells appear to be amorphous. Nevertheless, future investigations may focus on analyzing the short range order on greater detail and attempting to answer the question whether or not the simulated systems are true glasses. As a proposed strategy, simulations with a slower cooling rate could be employed to extract and plot total energy as a function of temperature. In case of a true glass, which would exhibit a liquid-glass transition, a change in slope will be visible. This methodology was already applied successfully to the InP system [169] and to a Zr-based metallic glass [170]. Initial results for the $Co_{43}Fe_{20}Ta_{5.5}B_{31.5}$ configuration indicate the presence of a kink in the energy-temperature curve at about 1000 K and hence the presence of a liquid-glass transition (see Figure 5-1).
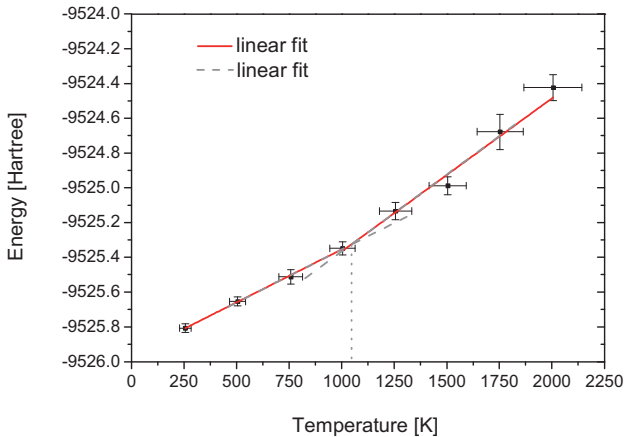

Figure 5-1: *Initial results for $Co_{43}Fe_{20}Ta_{5.5}B_{31.5}$ with a modeled cooling rate of $1.17x10^{14}$ K/s: Total energy is plotted versus temperature.*

Conclusions

Differential scanning calorimetry measurements to further evaluate the theoretical prediction and to enable comparability to literature data of glass transition temperatures are also suggested.

Since the here presented *ab-initio* model already includes all data needed for a time dependent analysis, it offers great potential to identify the underlying physical mechanisms of the liquid-glass transition. The analysis should focus on time dependent changes of (partial) PDFs [47, 170], coordination numbers and angular distributions.

Since the Si-containing glass revealed an outstanding relationship between density, bond length and coordination numbers compared to the systems with X=B, P and S, (the Co-Fe-Ta-Si system indicated a non-uniform packaging of clusters and cavities), a further, more detailed analysis of this glass plights interesting results. Employing similar PDF analysis as conducted here for $Co_{45.5}Fe_{24}Ta_6B_{24.5}$ or positron annihilation spectroscopy (PAS) data (examining open volume on sub-atomic length scales) may allow for the evaluation of the here presented theoretical description of density and atomic coordination for Co-Fe-Ta-Si. Similar studies are already reported for $Zr_{52.5}Ti_5Al_{10}Cu_{17.9}Ni_{14.6}$ [171], $Zr_{41.25}Ti_{13.75}Cu_{12.5}Ni_{10}Be_{22.5}$ [172] and $Zr_{58.5}Cu_{15.6}Ni_{12.8}Al_{10.3}Nb_{2.8}$ [173] metallic glasses. The already aforementioned DSC experiments may also provide further information related on cavities present in a glass: A monotonous relationship between the height of the glass transition peak and the amount of free volume is found for $Pd_{40}Ni_{40}P_{20}$ [174].

To pursue the here presented, promising methodology of metallic glass design, a further study on the impact of transition metal substitution/addition on the network-like structure Co-based metallic glasses are known for [39] and hence on structure and elasticity could be carried out. Initial results are obtained by Yao et al. [175] by substituting Ta with Nb. Further substitutions, analogous to the valence-electron-concentration and size variation presented here, could involve Zr or Mo. The effect of 2 at% Mo addition on the mechanical properties is already investigated for the Co-Fe-Ta-B bulk metallic glass [41].

6 REFERENCES

1. Klement, W., R.H. Willens, and P. Duwez, *Non-crystalline structure in solidified gold-silicon alloys.* Nature, 1960. **187**(4740): p. 869-870.

2. Chen, H.S. and D. Turnbull, *Evidence of a glass-liquid transition in a gold-germanium-silicon alloy* Journal of Chemical Physics, 1968. **48**(6): p. 2560.

3. Chen, H.S. and D. Turnbull, *Formation, stability and structure of palladium-silicon based alloy glasses.* Acta Metallurgica, 1969. **17**(8): p. 1021.

4. Chen, H.S., *Thermodynamic considerations on formation and stability of metallic glasses.* Acta Metallurgica, 1974. **22**(12): p. 1505-1511.

5. Kui, H.W., A.L. Greer, and D. Turnbull, *Formation of bulk metallic-glass by fluxing.* Applied Physics Letters, 1984. **45**(6): p. 615-616.

6. Inoue, A. and N. Nishiyama, *Extremely low critical cooling rates of new Pd-Cu-P base amorphous alloys.* Materials Science and Engineering a-Structural Materials Properties Microstructure and Processing, 1997. **226**: p. 401-405.

7. Inoue, A., N. Nishiyama, and H. Kimura, *Preparation and thermal stability of bulk amorphous Pd40Cu30Ni10P20 alloy cylinder of 72 mm in diameter.* Materials Transactions Jim, 1997. **38**(2): p. 179-183.

8. Inoue, A., et al., *Al-La-Cu amorphous-alloys with a wide supercooled liquid region.* Materials Transactions Jim, 1990. **31**(2): p. 104-109.

9. Johnson, W.L., *Bulk glass-forming metallic alloys: Science and technology.* Mrs Bulletin, 1999. **24**(10): p. 42-56.

10. Hays, C.C., C.P. Kim, and W.L. Johnson, *Large supercooled liquid region and phase separation in the Zr-Ti-Ni-Cu-Be bulk metallic glasses.* Applied Physics Letters, 1999. **75**(8): p. 1089-1091.

11. Schroers, J., *The Superplastic Forming of Bulk Metallic Glasses.* JOM, 2005. **5**: p. 34.

12. Schroers, J., et al., *Blow molding of bulk metallic glass.* Scripta Materialia, 2007. **57**(4): p. 341-344.

13. Telford, M., *The case for bulk metallic glass.* Materials Today, 2004. **7**(3): p. 36-43.

14. Sakurai, J., et al., *Combinatorial Search for Ni-Nb-Ti Thin Film Amorphous Alloys with High Corrosion Resistances.* Japanese Journal of Applied Physics, 2011. **50**(8): p. 6.

15. Kumar, G., H.X. Tang, and J. Schroers, *Nanomoulding with amorphous metals.* Nature, 2009. **457**(7231): p. 868-872.

16. Kakiuchi, H., et al., *Application of Zr-based bulk glassy alloys to golf clubs.* Materials Transactions, 2001. **42**(4): p. 678-681.

17. Hindmarch, A.T., et al., *Origin of in-plane uniaxial magnetic anisotropy in CoFeB amorphous ferromagnetic thin films.* Physical Review B, 2011. **83**(21): p. 212404.

18. Sharma, P., H. Kimura, and A. Inoue, *Observation of unusual magnetic behavior: Spin reorientation transition in thick Co-Fe-Ta-B glassy films.* Journal of Applied Physics, 2006. **100**(8): p. 083902.

19. Sharma, P., et al., *Temperature and thickness driven spin-reorientation transition in amorphous Co-Fe-Ta-B thin films.* Physical Review B, 2006. **73**(5): p. 052401.

20. Chen, L.H., et al., *Ultrahigh frequency properties of amorphous Co-Fe-Zr-B thin films* IEEE Transactions on Magnetics, 2001. **37**(4): p. 2242-2244.

21. Deng, Y.P., et al., *A combinatorial thin film sputtering approach for synthesizing and characterizing ternary ZrCuAl metallic glasses.* Intermetallics, 2007. **15**(9): p. 1208-1216.

22. Yamauchi, R., et al., *Combinatorial Search for Low Resistivity Pd-Cu-Si Thin Film Metallic Glass Compositions.* Japanese Journal of Applied Physics, 2006. **45**(7): p. 5911-5919.

References

23. Iljinas, A., D. Milčius, and J. Dudonis, *Deposition of amorphous Fe-Zr alloys by magnetron co-sputtering.* Vacuum, 2007. **81**(10): p. 1213-1215.

24. Liu, Y., et al., *Thermal, Mechanical and Electrical Properties of Pd-Based Thin-Film Metallic Glass.* Japanese Journal of Applied Physics, 2001. **40**(Part 1, No. 9A): p. 5382-5388.

25. Sharma, P., et al., *L1(0) FePt(111)/glassy CoFeTaB bilayered structure for patterned media.* Journal of Applied Physics, 2011. **109**(7): p. 07B908.

26. Jeong, H.-W., S. Hata, and A. Shimokohbe, *Microforming of three-dimensional microstructures from thin-film metallic glass.* Journal of Microelectromechanical Systems 2003. **12**(1): p. 42-52.

27. He, G., J. Eckert, and W. Löser, *Stability, phase transformation and deformation behavior of Ti-base metallic glass and composites.* Acta Materialia, 2003. **51**(6): p. 1621-1631.

28. Szuecs, F., C.P. Kim, and W.L. Johnson, *Mechanical properties of Zr56.2Ti13.8Nb5.0Cu6.9Ni5.6Be12.5 ductile phase reinforced bulk metallic glass composite.* Acta Materialia, 2001. **49**(9): p. 1507-1513.

29. Siegrist, M.E., D.P. Steinlin, and J.F. Löffler, *Processing of diamond-reinforced bulk metallic glass composites.* Materials Science and Engineering: A, 2007. **447**(1-2): p. 298-302.

30. Choi-Yim, H., et al., *Synthesis and characterization of particulate reinforced Zr57Nb5Al10Cu15.4Ni12.6 bulk metallic glass composites.* Acta Materialia, 1999. **47**(8): p. 2455-2462.

31. Eckert, J., A. Kübler, and L. Schultz, *Mechanically alloyed Zr55Al10Cu30Ni5 metallic glass composites containing nanocrystalline W particles.* Journal of Applied Physics, 1999. **85**(10): p. 7112-7119.

32. Conner, R.D., R.B. Dandliker, and W.L. Johnson, *Mechanical properties of tungsten and steel fiber reinforced Zr41.25Ti13.75Cu12.5Ni10Be22.5 metallic glass matrix composites.* Acta Materialia, 1998. **46**(17): p. 6089-6102.

33. Kim, C.P., et al., *Processing of carbon-fiber-reinforced Zr41.2Ti13.8Cu12.5Ni10.0Be22.5 bulk metallic glass composites.* Applied Physics Letters, 2001. **79**(10): p. 1456-1458.

34. Chen, H.S., *Metallic glasses.* Chinese Journal of Physics, 1990. **28**(5): p. 407-425.

35. Yoshida, S., et al., *Preparation of new amorphous powder cores using Fe-based glassy alloy.* Ieee Transactions on Magnetics, 2000. **36**(5): p. 3424-3429.

36. Inoue, A., *Bulk glassy and nonequilibrium crystalline alloys by stabilization of supercooled liquid: fabrication, functional properties and applications (Part 2).* Proc. Jpn. Acad., Ser. B, 2005. **81**: p. 172-188.

37. Löffler, J.F., *Bulk metallic glasses.* Intermetallics, 2003. **11**(6): p. 529-540.

38. Ramamurty, U., et al., *Hardness and plastic deformation in a bulk metallic glass.* Acta Materialia, 2005. **53**(3): p. 705-717.

39. Inoue, A., B.L. Shen, and C.T. Chang, *Fe- and Co-based bulk glassy alloys with ultrahigh strength of over 4000 MPa.* Intermetallics, 2006. **14**(8-9): p. 936-944.

40. Sharma, P., H. Kimura, and A. Inoue, *Tailoring the magnetic properties of mechanically hardest Co-Fe-Ta-B glassy thin films.* Journal of Applied Physics, 2007. **101**(9): p. 09N502.

41. Shen, B. and A. Inoue, *Enhancement of the fracture strength and glass-forming ability of CoFeTaB bulk glassy alloy.* Journal of Physics: Condensed Matter, 2005. **17**(37): p. 5647.

42. Xing, L.Q., et al., *Improved Al-Y-Fe glass formation by microalloying with Ti.* Philosophical Magazine Letters, 2004. **84**(5): p. 293-302.

43. Lu, B.-C., et al., *A model of atom dense packing for metallic glasses with high-solute concentration.* Applied Physics Letters, 2009. **94**(24): p. 241913.

44. Miracle, D.B., *A structural model for metallic glasses.* Nature Materials, 2004. **3**(10): p. 697-702.

45.   Miracle, D.B., *The efficient cluster packing model - An atomic structural model for metallic glasses.* Acta Materialia, 2006. **54**(16): p. 4317-4336.

46.   Lee, G.W., et al., *Difference in Icosahedral Short-Range Order in Early and Late Transition Metal Liquids.* Physical Review Letters, 2004. **93**(3): p. 037802.

47.   Sheng, H.W., et al., *Atomic packing and short-to-medium-range order in metallic glasses.* Nature, 2006. **439**(7075): p. 419-425.

48.   Mattern, N., et al., *Short-range order of Cu-Zr metallic glasses.* Journal of Alloys and Compounds, 2009. **485**(1-2): p. 163-169.

49.   Kaban, I., et al., *Topological and chemical ordering in Co43Fe20Ta5.5B31.5 metallic glass.* Physical Review B, 2009. **79**(21): p. 212201.

50.   Allen, M.P. and D.J. Tildersley, *Computer simulation of liquids.* 1989, Oxford: Oxford University Press.

51.   McGreevy, R.L., *Reverse Monte Carlo modelling.* Journal of Physics: Condensed Matter, 2001. **13**(46): p. R877.

52.   Hohenberg, P. and W. Kohn, *Inhomogeneous Electron Gas.* Physical Review, 1964. **136**(3B): p. B864.

53.   Kresse, G. and D. Joubert, *From ultrasoft pseudopotentials to the projector augmented-wave method.* Physical Review B, 1999. **59**(3): p. 1758-1775.

54.   Blöchl, P.E., *Projector augmented-wave method* Physical Review B, 1994. **50**(24): p. 17953-17979.

55.   Cui, Y.Y., et al., *Interatomic potential to calculate the driving force, optimized composition, and atomic structure of the Cu-Hf-Al metallic glasses.* **99**: p. 011911.

56.   He, Q., et al., *Locating bulk metallic glasses with high fracture toughness: Chemical effects and composition optimization.* Acta Materialia, 2011. **59**(1): p. 202-215.

57.   Dai, Y., J. Li, and B. Liu, *Glass-forming ability and atomic-level structure of the ternary Ag-Ni-Zr metallic glasses studied by molecular dynamics simulations.* Journal of Applied Physics, 2011. **109**(5): p. 053505.

58.   Matsuura, M., et al., *Local atomic structure of Ni(60)Pd(20)P(20) and Ni(60)Pd(20)P(17)B(3) bulk metallic glasses and the origin of glass forming ability.* Journal of Alloys and Compounds, 2010. **496**(1-2): p. 135-139.

59.   Laws, K.J., et al., *Prediction of Glass-Forming Compositions in Metallic Systems: Copper-Based Bulk Metallic Glasses in the Cu-Mg-Ca System.* Metallurgical and Materials Transactions a-Physical Metallurgy and Materials Science, 2010. **41A**(7): p. 1699-1705.

60.   Fukuhara, M., et al., *Electronic rule for formation of glassy alloys.* Applied Physics Letters, 2007. **90**(7): p. 073114.

61.   Kazimirov, V.Y., et al., *Local organization and atomic clustering in multicomponent amorphous steels.* Physical Review B, 2008. **78**(5): p. 054112.

62.   Kazimirov, V.Y., *First-principles simulation of the elastic properties of multicomponent amorphous steels.* Physical Review B, 2009. **80**(21): p. 214117.

63.   Sheng, H.W., et al., *Polyamorphism in a metallic glass.* Nat Mater, 2007. **6**(3): p. 192-197.

64.   Guerdane, M. and H. Teichler, *Structure of the amorphous, massive-metallic-glass forming Ni25Zr60Al15 alloy from molecular dynamics simulations.* Physical Review B, 2001. **65**(1): p. 014203.

65.   Imafuku, M., et al., *Structural study of Fe90-xNb10Bx (x=10, 20 and 30) glassy alloys.* Journal of Non-Crystalline Solids, 2002. **312-314**: p. 589-593.

66.   Qin, J.Y., et al., *Study on the structural relationship between the liquid and amorphous Fe78Si9B13 alloys by ab initio molecular dynamics simulation.* Applied Physics Letters, 2007. **90**(20): p. 201909.

References

67. Fang, H.Z., et al., *Al-centered icosahedral ordering in Cu(46)Zr(46)Al(8) bulk metallic glass.* Applied Physics Letters, 2009. **94**(9): p. 091904.

68. Hirata, A., et al., *Direct observation of local atomic order in a metallic glass.* Nat Mater, 2010. **10**(1): p. 28-33.

69. Pasturel, A. and N. Jakse, *Ab initio molecular dynamics to designing structural and dynamic properties in metallic glass-forming alloys.* Computational Materials Science. **49**(4): p. S210-S213.

70. Bernal, J.D., *Geometry of the structure of monatomic liquids* Nature, 1960. **185**(4706): p. 68-70.

71. Bernal, J.D., *Bakerian lecture 1962 - Structure of liquids.* Proceedings of the Royal Society of London Series A-Mathematical and Physical Sciences, 1964. **280**(1380): p. 299.

72. Polk, D.E., *Structure of glassy metallic alloys.* Acta Metallurgica, 1972. **20**(4): p. 485.

73. Gaskell, P.H., *New structural model for amorphous transition-metal silicides, borides, phosphides and carbides.* Journal of Non-Crystalline Solids, 1979. **32**(1-3): p. 207-224.

74. Miracle, D.B., *Efficient local packing in metallic glasses.* Journal of Non-Crystalline Solids, 2004. **342**(1-3): p. 89-96.

75. Miracle, D.B., W.S. Sanders, and O.N. Senkov, *The influence of efficient atomic packing on the constitution of metallic glasses.* Philosophical Magazine, 2003. **83**(20): p. 2409-2428.

76. Egami, T. and S. Billinge, *Underneath the Bragg Peaks: Structural analysis of complex materials*. Pergamon Press. 2003, Oxford, England: Elsevier.

77. Finney, J.L., *Modeling structures of amorphous metals and alloys.* Nature, 1977. **266**(5600): p. 309-314.

78. Clarke, A.S. and H. Jonsson, *Structural-changes accompanying densification of random hard-sphere packings.* Physical Review E, 1993. **47**(6): p. 3975-3984.

79. Barney, E.R., et al., *A neutron and X-ray diffraction study of Ca-Mg-Cu metallic glasses.* Intermetallics, 2011. **19**(7): p. 860-870.

80. Cockayne, D.J.H., *The study of nanovolumes of amorphous materials using electron scattering*, in *Annual Review of Materials Research*. 2007, Annual Reviews: Palo Alto. p. 159-187.

81. García-Arribas, A., M.L. Fdez-Gubieda, and J.J. Rehr, *Influence of metalloids on the XANES spectra of metallic glasses.* Journal of Non-Crystalline Solids, 2001. **287**(1-3): p. 60-64.

82. Gibson, J.M., M.M.J. Treacy, and P.M. Voyles, *Atom pair persistence in disordered materials from fluctuation microscopy.* Ultramicroscopy, 2000. **83**: p. 169-178.

83. Voyles, P.M. and J.R. Abelson, *Medium-range order in amorphous silicon measured by fluctuation electron microscopy.* Solar Energy Materials and Solar Cells, 2003. **78**(1-4): p. 85-113.

84. Ashby, M.F. and A.L. Greer, *Metallic glasses as structural materials.* Scripta Materialia, 2006. **54**(3): p. 321-326.

85. Conner, R.D., et al., *Fracture toughness determination for a beryllium-bearing bulk metallic glass.* Scripta Materialia, 1997. **37**(9): p. 1373-1378.

86. Wang, W.H., C. Dong, and C.H. Shek, *Bulk metallic glasses.* Materials Science & Engineering R-Reports, 2004. **44**(2-3): p. 45-89.

87. Inoue, A., A. Makino, and T. Mizushima, *Ferromagnetic bulk glassy alloys.* Journal of Magnetism and Magnetic Materials, 2000. **215-216**(0): p. 246-252.

88. Inoue, A., *Stabilization of metallic supercooled liquid and bulk amorphous alloys.* Acta Materialia, 2000. **48**(1): p. 279-306.

89. Inoue, A. and R.E. Park, *Soft Magnetic Properties and Wide Supercooled Liquid Region of Fe-P-B-Si Base Amorphous Alloys.* Materials Transactions Jim, 1996. **37**(11): p. 1715-1721.

90.   Nishiyama, N., K. Amiya, and A. Inoue. *Bulk metallic glasses for industrial products; New structural and functional applications*. in *Symposium on Amorphous and Nanocrystalline Metals held at the 2003 MRS Fall Meeting*. 2004. Boston, MA: Materials Research Society, 506 Keystone Drive, Warrendale, PA 15088-7563 USA.

91.   Inoue, A., et al., *Cobalt-based bulk glassy alloy with ultrahigh strength and soft magnetic properties.* Nat Mater, 2003. **2**(10): p. 661-663.

92.   Inoue, A., et al., *Ferromagnetic Co-Fe-Zr-B amorphous alloys with glass transition and good high-frequency permeability.* Applied Physics Letters, 1998. **73**(6): p. 744-746.

93.   Inoue, A., et al., *New bulk amorphous Fe-(Co,Ni)-M-B (M=Zr,Hf,Nb,Ta,Mo,W) alloys with good soft magnetic properties.* Journal of Applied Physics, 1998. **83**(11): p. 6326-6328.

94.   Fornell, J., et al., *Enhanced mechanical properties due to structural changes induced by devitrification in Fe-Co-B-Si-Nb bulk metallic glass.* Acta Materialia, 2010. **58**(19): p. 6256-6266.

95.   Hirata, A., et al., *Nanocrystallization of complex Fe23B6-type structure in glassy Fe-Co-B-Si-Nb alloy.* Intermetallics, 2008. **16**(4): p. 491-497.

96.   Man, Q.K., et al., *Enhancement of glass-forming ability of CoFeBSiNb bulk glassy alloys with excellent soft-magnetic properties and superhigh strength.* Intermetallics, 2010. **18**(10): p. 1876-1879.

97.   Itoi, T. and A. Inoue, *Thermal stability and soft magnetic properties of Co-Fe-M-B (M=Nb, Zr) amorphous alloys with large supercooled liquid region.* Materials Transactions Jim, 2000. **41**(9): p. 1256-1262.

98.   Rho, I.C., et al., *Microstructure and crystallization kinetics of amorphous metallic alloy: Fe54Co26Si6B14.* Journal of Non-Crystalline Solids, 2003. **316**(2-3): p. 289-296.

99.   Chang, Z.Y., et al., *Catching Fe-based bulk metallic glass with combination of high glass forming ability, ultrahigh strength and good plasticity in Fe-Co-Nb-B system.* Materials Science and Engineering: A, 2009. **517**(1-2): p. 246-248.

100.   Huaijun, S., et al., *Effects of B and Si contents on glass-forming ability and soft-magnetic properties in (Co 0.89Fe 0.057Nb 0.053) 100-x(B 0.8Si 0.2) x glassy alloys.* Journal of Applied Physics, 2010. **107**(9): p. 09A319.

101.   Man, Q., et al., *Enhancement of glass-forming ability of CoFeBSiNb bulk glassy alloys with excellent soft-magnetic properties and superhigh strength.* Intermetallics. **18**(10): p. 1876-1879.

102.   Imafuku, M., et al., *Crystallization behavior of amorphous Fe90-XNb10BX (X = 10 and 38) alloys.* Materials Transactions Jim, 2000. **41**(11): p. 1526-1529.

103.   Inoue, A., et al., *Ultra-high strength above 5000 MPa and soft magnetic properties of Co-Fe-Ta-B bulk glassy alloys.* Acta Materialia, 2004. **52**(6): p. 1631-1637.

104.   Hostert, C., et al., *Ab-initio molecular dynamics model for density, elastic properties and short range order of Co-Fe-Ta-B metallic glass thin films.* Journal of Physics: Condensed Matter, 2011. **23**(47): p. 475401.

105.   Wang, J., et al., *Compressibility and hardness of Co-based bulk metallic glass: A combined experimental and density functional theory study.* Applied Physics Letters, 2011. **99**(15): p. 151911.

106.   Mihalkovic, M. and M. Widom, *Ab initio calculations of cohesive energies of Fe-based glass-forming alloys.* Physical Review B, 2004. **70**(14): p. 144107.

107.   He, Q., et al., *Locating bulk metallic glasses with high fracture toughness: Chemical effects and composition optimization.* Acta Materialia, 2010. **59**(1): p. 202-215.

108.   Shen, B., et al., *Corrosion properties of Co43Fe20Ta5.5B31.5 bulk glassy alloy.* Journal of Alloys and Compounds, 2008. **460**(1-2): p. L11-L13.

References

109. de Oliveira, M.F., et al., *Glass formation of alloys selected by lambda and electronegativity criteria in the Ti-Zr-Fe-Co system.* Journal of Alloys and Compounds, 2010. **495**(2): p. 316-318.

110. Hostert, C., et al., *Density, elastic and magnetic properties of Co-Fe-Ta-Si metallic glasses by theory and experiment.* Scripta Materialia, 2012. **66**(10): p. 765-768.

111. Makino, A., et al., *FeSiBP bulk metallic glasses with high magnetization and excellent magnetic softness.* Journal of Magnetism and Magnetic Materials, 2008. **320**(20): p. 2499-2503.

112. Li, H.X. and S. Yi, *Fabrication of bulk metallic glasses in the alloy system Fe-C-Si-B-P-Cr-Mo-Al using hot metal and industrial ferro-alloys.* Materials Science and Engineering a-Structural Materials Properties Microstructure and Processing, 2007. **449**: p. 189-192.

113. Cui, Y.Y., et al., *Interatomic potential to calculate the driving force, optimized composition, and atomic structure of the Cu-Hf-Al metallic glasses.* Applied Physics Letters, 2011. **99**(1): p. 011911.

114. Pasturel, A. and N. Jakse, *Ab initio molecular dynamics to designing structural and dynamic properties in metallic glass-forming alloys.* Computational Materials Science, 2010. **49**(4, Supplement 1): p. S210-S213.

115. Sakurai, J.J., *Modern Quantum Mechanics.* 1994: Addison Wesley Professional.

116. Sholl, D.S. and J.A. Steckel, *Density functional theory: a practical introduction.* 2009, Hoboken, New Jersey: John Wiley & Sons, Inc.

117. Hohenberg, P. and W. Kohn, *Inhomogeneous electron gas.* Physical Review B, 1964. **136**(3B): p. B864.

118. Kohn, W. and L.J. Sham, *Self-consistent equations including exchange and correlation effects.* Physical Review, 1965. **140**(4A): p. A1133-A1138.

119. Perdew, J.P. and Y. Wang, *Accurate and simple analytic representation of the electron-gas correlation-energy.* Physical Review B, 1992. **45**(23): p. 13244-13249.

120. Perdew, J.P., K. Burke, and M. Ernzerhof, *Generalized gradient approximation made simple.* Physical Review Letters, 1996. **77**(18): p. 3865-3868.

121. Kresse, G. and J. Hafner, *Ab-initio molecular-dynamics simulation of the liquid-metal amorphous-semiconductor transition in germanium.* Physical Review B, 1994. **49**(20): p. 14251-14269.

122. Ozaki, T. and H. Kino, *Efficient projector expansion for the ab initio LCAO method.* Physical Review B, 2005. **72**(4): p. 045121.

123. *OpenMX version 3.5 was used in this study and is available at* www.openmx-square.org.

124. Ozaki, T., *Variationally optimized atomic orbitals for large-scale electronic structures.* Physical Review B, 2003. **67**(15): p. 155108.

125. Barbee Jr, T.W., et al., *Synthesis of amorphous niobium-nickel alloys by vapor quenching.* Thin Solid Films, 1977. **45**(3): p. 591-599.

126. Vosko, S.H., L. Wilk, and M. Nusair, *Accurate spin-dependent electron liquid correlation energies for local spin-density calculations - a critical analysis.* Canadian Journal of Physics, 1980. **58**(8): p. 1200-1211.

127. Monkhorst, H.J. and J.D. Pack, *Special points for Brillouin-zone integrations.* Physical Review B, 1976. **13**(12): p. 5188-5192.

128. Blöchl, P.E., O. Jepsen, and O.K. Andersen, *Improved tetrahedron method for Brillouin-zone integrations.* Physical Review B, 1994. **49**(23): p. 16223-16233.

129. Birch, F., *Finite strain isotherm and velocities for single-crystal and polycrystalline NaCl at high-pressures and 300-degree-K.* Journal of Geophysical Research, 1978. **83**(NB3): p. 1257-1268.

130.   Allred, A.L. and E.G. Rochow, *A SCALE OF ELECTRONEGATIVITY BASED ON ELECTROSTATIC FORCE.* Journal of Inorganic & Nuclear Chemistry, 1958. **5**(4): p. 264-268.

131.   Bader, R.F.W., *Atoms in Molecules: A Quantum Theory*. The International Series of Monographs on Chemistry. Vol. No 22. 1990: Oxford University Press.

132.   Henkelman, G., A. Arnaldsson, and H. Jonsson, *A fast and robust algorithm for Bader decomposition of charge density.* Computational Materials Science, 2006. **36**(3): p. 354-360.

133.   Tang, W., E. Sanville, and G. Henkelman, *A grid-based Bader analysis algorithm without lattice bias.* Journal of Physics-Condensed Matter, 2009. **21**(8): p. 084204.

134.   Jing, Q., et al., *Zr-Cu amorphous films prepared by magnetron Co-sputtering deposition of pure Zr and Cu.* Chinese Physics Letters, 2009. **26**(8): p. 086109.

135.   Ohring, M., *Materials Science of Thin Films - Deposition & Structure*. 2002, San Diego: Academic Press.

136.   Smith, D.L., *Thin-Film Deposition - Principles and Practice*. 1995, Boston: McGraw-Hill.

137.   Gebhardt, T., et al., *Influence of chemical composition and magnetic effects on the elastic properties of fcc Fe-Mn alloys.* Acta Materialia, 2010. **59**(4): p. 1493-1501.

138.   Kelly, T.F. and M.K. Miller, *Invited review article: Atom probe tomography.* Review of Scientific Instruments, 2007. **78**(3).

139.   Seidman, D.N., *Three-dimensional atom-probe tomography: Advances and applications*. Annual Review of Materials Research. Vol. 37. 2007. 127-158.

140.   Sun, Z., J. Zhou, and R. Ahuja, *Unique Melting Behavior in Phase-Change Materials for Rewritable Data Storage.* Physical Review Letters, 2007. **98**(5): p. 055505.

141.   Hammersley, A.P., et al., *Two-dimensional detector software: From real detector to idealised image or two-theta scan*. High Pressure Research. Vol. 14. 1996: Taylor & Francis.

142.   Birkholz, M., *Thin film analysis by X-ray scattering*. 2006, Weinheim: Wiley-VCH.

143.   Holy, V., et al., *X-ray reflection from rough layered systems.* Physical Review B, 1993. **47**(23): p. 15896-15903.

144.   Als-Nielsen, J., *Elements of Modern X-Ray Physics*. 2001, New York: Wiley.

145.   Bjorck, M. and G. Andersson, *GenX: an extensible X-ray reflectivity refinement program utilizing differential evolution.* Journal of Applied Crystallography, 2007. **40**(6): p. 1174-1178.

146.   Oliver, W.C. and G.M. Pharr, *An improved technique for determining hardness and elastic-modulus using load and displacement sensing indentation experiments.* Journal of Materials Research, 1992. **7**(6): p. 1564-1583.

147.   Fischer-Cripps, A.C., *Nanoindentation*. 2004, New York: Springer Science + Business Media.

148.   Dugdale, J.S. and D.K.C. MacDonald, *The Thermal Expansion of Solids.* Physical Review, 1953. **89**(4): p. 832.

149.   Eriksson, O., *Encyclopedia of Materials: Science and technology*. 2006: Elsevier.

150.   Schneider, J.M., et al., *Role of hydrogen for the elastic properties of alumina thin films.* Applied Physics Letters, 2002. **80**(7): p. 1144-1146.

151.   Hongyou, F., et al., *Modulus-density scaling behaviour and framework architecture of nanoporous self-assembled silicas.* Nature Materials, 2007. **6**(6).

152.   ElKhakani, M.A., et al., *Linear dependence of both the hardness and the elastic modulus of pulsed laser deposited a-SiC films upon their Si-C bond density.* Journal of Applied Physics, 1997. **82**(9): p. 4310-4318.

References

153. Music, D. and J.M. Schneider, *Elastic properties of amorphous boron suboxide based solids studied using ab-initio molecular dynamics.* Journal of Physics: Condensed Matter, 2008. **20**(19): p. 195203.

154. Music, D., et al., *Elastic modulus-density relationship for amorphous boron suboxide thin films.* Applied Physics A: Materials Science & Processing, 2003. **76**(2): p. 269-271.

155. Ozaki, T. and H. Kino, *Numerical atomic basis orbitals from H to Kr.* Physical Review B, 2004. **69**(19): p. 195113.

156. Momma, K. and F. Izumi, *VESTA: a three-dimensional visualization system for electronic and structural analysis.* Journal of Applied Crystallography, 2008. **41**: p. 653-658.

157. Pusztai, L. and E. Svab, *Modeling the structure of Ni65B35 metallic-glass by Reverse Monte-Carlo simulation.* Journal of Physics-Condensed Matter, 1993. **5**(47): p. 8815-8828.

158. Greenwood, N.N., R.V. Parish, and P. Thornton, *Metal borides.* Quarterly Reviews, 1966. **20**(3): p. 441-464.

159. Shannon, R.D., *Revised effective ionic-radii and and systematic studies of interatomic distances in halides and chalcogenides.* Acta Crystallographica Section A, 1976. **32**(SEP1): p. 751-767.

160. Kurapov, D., et al., *Influence of the normalized ion flux on the constitution of alumina films deposited by plasma-assisted chemical vapor deposition.* Journal of Vacuum Science & Technology A: Vacuum, Surfaces, and Films, 2007. **25**(4): p. 831-836.

161. Kittel, C., *Introduction to solid state physics*. 8 ed. 2005: Wiley.

162. Egami, T., *Magnetic amorphous alloys: physics and technological applications.* Reports on Progress in Physics, 1984. **47**(12): p. 1601.

163. Alben, R.A., J.I. Budnick, and G.S. Cargill, *Metallic Glasses*, ed. J.J.G.a.H.J. Leamy. Vol. III. 1978, Ohio: Metals Park, ASM.

164. Chen, H.S., *Correlation between elastic constants and flow behavior in metallic glasses.* Journal of Applied Physics, 1978. **49**(1): p. 462-463.

165. Cartledge, G.H., *Studies on the periodic system. II. The ionic potenial and related properties 1* Journal of the American Chemical Society, 1928. **50**(11): p. 2863-2872.

166. Cartledge, G.H., *Studies on the periodic system. III. The relation between ionizing potentials and ionic potentials.* Journal of the American Chemical Society, 1930. **52**(8): p. 3076-3083.

167. Rayner-Canham, G., *Periodic patterns.* Journal of Chemical Education, 2000. **77**(8): p. 1053-1056.

168. Zdetsis, A.D., *Designing novel Sn-Bi, Si-C and Ge-C nanostructures, using simple theoretical chemical similarities.* Nanoscale Research Letters, 2011. **6**: p. 362.

169. Lewis, L.J., A. De Vita, and R. Car, *Structure and electronic properties of amorphous indium phosphide from first principles.* Physical Review B, 1998. **57**(3): p. 1594-1606.

170. Hui, X., et al., *Atomic structure of Zr(41.2)Ti(13.8)Cu(12.5)Ni(10)Be(22.5) bulk metallic glass alloy.* Acta Materialia, 2009. **57**(2): p. 376-391.

171. Asoka-Kumar, P., et al., *Chemical ordering around open-volume regions in bulk metallic glass Zr52.5Ti5Al10Cu17.9Ni14.6.* Applied Physics Letters, 2000. **77**(13): p. 1973-1975.

172. Flores, K.M., et al., *Characterization of Free Volume in a Bulk Metallic Glass Using Positron Annihilation Spectroscopy.* Journal of Materials Research, 2002. **17**: p. 1153-1161.

173. Flores, K.M., et al., *Sub-nanometer open volume regions in a bulk metallic glass investigated by positron annihilation.* Acta Materialia, 2007. **55**(10): p. 3403-3411.

174. Tuinstra, P., et al., *The calorimetric glass transition of amorphous Pd40Ni40P20.* Acta Metallurgica et Materialia, 1995. **43**(7): p. 2815-2823.

175. Yao, J.H., et al., *Ab initio molecular dynamics model for density, elastic properties and short range order of Co-Fe-Nb-B metallic glass thin films.* In preparation.

7 CURRICULUM VITAE

Carolin Hildegard Hostert
Born in Aachen, Germany on 20.08.1982
Nationality: German

04/2007 – 12/2011
PhD student and research assistant at Lehrstuhl für Werkstoffchemie (MCh), RWTH Aachen University, Germany

04/05 – 04/07
„Materials science" master studies at RWTH Aachen University, Germany
Title master thesis: „Structure Chemistry and Adhesion of Cr_2AlC and V_2AlC Thin Films"
Degree: Master of Science (M.Sc.)

10/01 – 04/05
„Materials science" bachelor studies at RWTH Aachen University, Germany
Title bachelor thesis: „Gelbildung und Charakterisierung von Stern-PEO-Hydrogelen"
Degree: Bachelor of Science (B.Sc.)

1992 – 2001
Secondary school *St. Leonhard*, Aachen, Germany
Degree: general qualification for university entrance

1988 – 1992
Primary school *Gemeinschaftsgrundschule Saarstraße*, Aachen, Germany